Monthly Notices of the ROYAL ASTRONOMICAL SOCIETY

MNRAS **502,** 108–126 (2021) doi:10.1093/mnras/stab070
Advance Access publication 2021 January 13

IGM transmission bias for $z \geq 2.9$ Lyman continuum detected galaxies

R. Bassett,[1,2]★ E. V. Ryan-Weber,[1,2] J. Cooke,[1,2] U. Meštrić,[1,2] K. Kakiichi,[3,4] L. Prichard[5] and M. Rafelski[5,6]

[1]*Centre for Astrophysics and Supercomputing, Swinburne University of Technology, PO Box 218, Hawthorn VIC 3122, Australia*
[2]*ARC Centre of Excellence for All Sky Astrophysics in 3 Dimensions (ASTRO 3D), Australia*
[3]*Department of Physics, University of California, Santa Barbara, CA 93106, USA*
[4]*Department of Physics and Astronomy, University College London, London, WC1E 6BT, UK*
[5]*Space Telescope Science Institute, 3700 San Martin Drive, Baltimore MD 21218, USA*
[6]*Department of Physics & Astronomy, John Hopkins University, Baltimore, MD 21218, USA*

Accepted 2021 January 5. Received 2021 January 4; in original form 2020 October 21

ABSTRACT

Understanding the relationship between the underlying escape fraction of Lyman continuum (LyC) photons ($f_{\rm esc}$) emitted by galaxies and measuring the distribution of observed $f_{\rm esc}$ values at high redshift is fundamental to the interpretation of the reionization process. In this paper, we perform a statistical exploration of the attenuation of LyC photons by neutral hydrogen in the intergalactic medium using ensembles of simulated transmission functions. We show that LyC-detected galaxies are more likely to be found in sightlines with higher than average transmission of LyC photons. This means that adopting a mean transmission at a given redshift leads to an overestimate of the true $f_{\rm esc}$ for LyC-detected galaxies. We note, however, that mean values are appropriate for $f_{\rm esc}$ estimates of larger parent samples that include LyC non-detected galaxies. We quantify this IGM transmission bias for LyC detections in photometric and spectroscopic surveys in the literature and show that the bias is stronger for both shallower observations and for fainter parent samples (i.e. Ly α emitters versus Lyman break galaxies). We also explore the effects of varying the underlying probability distribution function (PDF) of $f_{\rm esc}$ on recovered values, showing that the underlying $f_{\rm esc}$ PDF may depend on sample selection by comparing with observational surveys. This work represents a first step in improved interpretation of LyC detections in the context of understanding $f_{\rm esc}$ from high-redshift galaxies.

Key words: intergalactic medium – galaxies: ISM – dark ages, reionization, first stars.

1 INTRODUCTION

Understanding the details of cosmic reionization, the epoch at $z \simeq 6$–10, during which the hydrogen content of the intergalactic medium (IGM) transitioned from neutral to mostly ionized (e.g. Fan, Carilli & Keating 2006; Planck Collaboration XLVI 2016; Greig & Mesinger 2017; Mason et al. 2018), is a major goal of the international astronomical community. The general consensus currently favours a picture in which ionizing, or Lyman continuum (LyC), photons originating from young, massive stars and/or X-ray binaries and Wolf–Rayet stars in star-forming galaxies are the primary driver. This picture is supported by extensive theoretical (e.g. Wise & Cen 2009; Yajima, Choi & Nagamine 2011; Paardekooper, Khochfar & Dalla Vecchia 2015) and observational (e.g. Inoue, Iwata & Deharveng 2006; Ouchi et al. 2009; Robertson et al. 2015) efforts. Active galactic nuclei, though pridigious producers of LyC emission, are expected to play only a minor role due to their low number density at $z > 6$ (e.g. Hopkins, Richards & Hernquist 2007; Kakiichi et al. 2018; Parsa, Dunlop & McLure 2018).

Detailed modelling of the reionization process critically requires an accurate census of the fraction of LyC photons (with respect to ultraviolet, UV, continuum photons) produced in galaxies that manage to escape into the IGM, typically referred to as the LyC escape fraction ($f_{\rm esc}$). The first major challenge in using $f_{\rm esc}$ to understand reionization is the fact that no LyC photons from galaxies during the Epoch of Reionization (EoR) will ever reach a telescope due to absorption from intervening hydrogen. The second is the inherent faintness of LyC emission from galaxies (as demonstrated by pioneering works of Giallongo et al. 2002; Fernández-Soto, Lanzetta & Chen 2003; Inoue et al. 2005), which is driven largely by two key factors.

The first factor driving the faintness of LyC emission is that $f_{\rm esc}$ is typically found to be very low (or zero) as inferred from the lack of LyC detections in, e.g. Boutsia et al. (2011), Japelj et al. (2017), and Bian & Fan (2020). This may, in part, be due to the fact that observations of galaxies, and thus, their LyC emission, at high redshift ($z \geq 2.9$) are limited to relatively high stellar mass ($M_* \geq 10^9$ M$_\odot$) galaxies that are likely to contain significant quantities of neutral hydrogen (consistent with their high star formation rates, SFRs, e.g. Steidel, Pettini & Adelberger 2001; Iwata et al. 2009; Nestor et al. 2011; Grazian et al. 2016) that absorbs ionizing radiation before it can enter the IGM and drive reionization. Indeed, for the small sample of such known LyC-emitting galaxies at $z \gtrsim 2.8$, the observed LyC flux is relatively faint (e.g. Shapley et al. 2006; Micheva et al. 2017; Vanzella et al. 2018). Even if $f_{\rm esc}$ is larger in lower mass galaxies, such galaxies are inherently faint and their LyC emission will likely be at least as difficult to detect as their higher mass counterparts

★ E-mail: rbassett@swin.edu.au

(apart from the rare cases of strong gravitational lensing; Bian et al. 2017; Rivera-Thorsen et al. 2019). The most straightforward way past this problem is to perform larger and deeper surveys targeting LyC emission across a range of redshifts. A variety such surveys are currently in progress.

The second issue resulting in faint LyC emission is that the IGM itself contains large fractions of neutral hydrogen above $z \simeq 3$ (e.g. Inoue et al. 2014). This means that after LyC escapes from a galaxy it is largely absorbed in the IGM before reaching the Earth. For any individual LyC detection, there is currently no reliable method for inferring the IGM transmission ($T_{\rm IGM}$) of LyC photons for that particular sightline. This is troubling as observationally $T_{\rm IGM}$ and $f_{\rm esc}$ are degenerate meaning that, in order to estimate $f_{\rm esc}$, a value of $T_{\rm IGM}$ must be assumed that may or may not be appropriate for a given IGM sightline. There is, however, hope of a way forward as the differential column density distribution of H I absorption systems is well constrained (e.g. Meiksin 2006; Becker et al. 2013; Rudie et al. 2013), providing a statistical description of the probability that LyC photons escaping galaxies will be absorbed by hydrogen in the IGM at a given redshift.

Such a statistical approach to estimate $T_{\rm IGM}$ in a theoretical context has been explored using Monte Carlo (MC) simulations for around three decades (e.g. Møller & Jakobsen 1990; Bershady, Charlton & Geoffroy 1999; Inoue et al. 2014). Similarly, the application of such MC simulations of $T_{\rm IGM}$ to detections (and non-detections) of LyC radiation has a long history (e.g. Shapley et al. 2006; Siana et al. 2007; Steidel et al. 2018, S18 hereafter) In general, the most probable value of $T_{\rm IGM}$ at $z > 3$ is zero, though individual sightlines with $T_{\rm IGM} > 0.8$ can exist (see Section 2.1. The typical probability distribution of $T_{\rm IGM}$ (around $\lambda_{\rm rest} \sim 910$ Å) at $z = 2.9$–4.0 can be described as bimodal with a sharp peak at $T_{\rm IGM} = 0.0$ and a broader, less prominent peak at higher values. Both the location and prominence of this secondary peak decrease with redshift until $z \sim 5-6$, at which point the presence of high $T_{\rm IGM}$ sightlines is negligible. The result is that LyC is unlikely to be observed from galaxies *during* the EoR.

Using knowledge of the probability distribution of $T_{\rm IGM}$ at a given redshift, astronomers can put forward an estimate of $f_{\rm esc}$ for LyC-detected galaxies. One method is to apply the full suite of $T_{\rm IGM}$ models to a given observation (or set of observations), however, this typically results in largely unconstrained $f_{\rm esc}$ values including a large number with the unphysical case of $f_{\rm esc} > 1.0$ (Shapley et al. 2016; Vanzella et al. 2016). Another method is to assume the mean value of $T_{\rm IGM}$, $\langle T_{\rm IGM} \rangle$, among all simulated sightlines thus providing a single $f_{\rm esc}$ value (S18, Bassett et al. 2019; Fletcher et al. 2019; Meštrić et al. 2020, hereafter F19 and M20). The problem with this second method is that a single statistic belies to complexities of the underlying $T_{\rm IGM}$ distribution. Indeed, the mean of a bimodal distribution will be found to lie between the two peaks, and will not fall among the most likely values. This issue has been highlighted in the context of Ly α transmission by Byrohl & Gronke (2020) who find that assuming a median or mean transmission curve 'is misleading and should be interpreted with caution'.

There exist, however, important observational priors that can provide more realistic constraints on the most likely value of $T_{\rm IGM}$ for LyC-detected galaxies. First and foremost, the fact that a galaxy has been detected at LyC wavelengths means that $T_{\rm IGM}$ for that galaxy *cannot* be zero. This fact automatically reduces the underlying bimodal $T_{\rm IGM}$ distribution for all sightlines to a unimodal distribution for sightlines with LyC detections. In this case, standard statistics such as the mean and median of $T_{\rm IGM}$ may be more applicable. Secondly, while the probability distribution function (PDF) of $T_{\rm IGM}$ is routinely considered, the underlying PDF of $f_{\rm esc}$ itself, which so far has been left out, may also be important. As we have stated, low or zero $f_{\rm esc}$ values seem to be preferred, which is not reflected in current $f_{\rm esc}$ calculations. It is possible that the broad behaviour of the $f_{\rm esc}$ PDF may be inferred through consideration of the detection rates in LyC surveys (this intriguing idea is explored further in Section 4.3). It is likely that a full understanding of the underlying $f_{\rm esc}$ PDF of galaxies will require a theoretical underpinning through the careful analysis of high-resolution, hydrodynamical simulations employing radiative transfer of ionizing photons (e.g. Trebitsch et al. 2017; Rosdahl et al. 2018; Ma et al. 2020).

In this paper, we explore in detail the probability distributions of both $T_{\rm IGM}$ and $f_{\rm esc}$ in the context of known LyC surveys at high redshift. Our goal is to provide a statistically sound framework within which astronomers can calculate meaningful estimates of $f_{\rm esc}$ for both individual LyC detections as well as stacked samples. In particular, we show that both the assumption of the mean $T_{\rm IGM}$ value and (to a lesser extent) a lack of consideration of the underlying $f_{\rm esc}$ PDF result in an overestimate of $f_{\rm esc}$ for LyC-detected galaxies. Here, we quantify the IGM transmission bias, $T_{\rm bias}$, as $\langle T_{\rm det} \rangle - \langle T_{\rm IGM} \rangle$, where $\langle T_{\rm det} \rangle$ is the average IGM transmission for LyC-detected galaxies for a given observational detection limit. We note that, although a transmission value is not inherently an additive quantity, our definition leads to a roughly redshift independent correction to $\langle T_{\rm IGM} \rangle$ as opposed to an alternative definition such as $T_{\rm bias} = \langle T_{\rm det} \rangle / \langle T_{\rm IGM} \rangle$ (see Section 3 for further discussion).

This paper is organized as follows: In Section 2, we describe our method of generating simulated IGM sightlines and spectra of mock LyC-emitting galaxies; in Section 3, we describe the results of our various models; in Section 4, we explore the implications of our results in the context of past and ongoing LyC surveys; and in Section 5 we provide a brief summary of our findings.

2 SIMULATING LYC-LEAKING GALAXIES

In this section, we describe our method of producing mock observations of LyC flux from high-redshift galaxies. There are three primary ingredients in creating an individual high-redshift galaxy observation for our simulation: an IGM transmission function, $f_{\rm esc}$, and the input Spectral Energy Distribution (SED) model. Our method for producing an IGM transmission function is described in Section 2.1. Although the underlying PDF of $f_{\rm esc}$ for galaxies is largely unknown, we test two models described in Section 2.2. Finally, we take our input SED model from BPASSv2.1 (described further in Section 2.3 Eldridge et al. 2017), matching the assumed LyC to non-ionizing UV flux ratio from previous studies. In particular, we compare with results from the Keck Lyman Continuum Survey (KLCS; S18), the LymAn Continuum Escape Survey (LACES; F19), and the ground-based photometric work of M20 based on deep *u*-band photometry from the Canada–France–Hawaii Telescope (CFHT) Large Area *U*-band Deep Survey (CLAUDS; Sawicki et al. 2019).

2.1 IGM transmission functions

$T_{\rm IGM}$ functions are produced following the method outlined in S18, Appendix B.[1] We perform a Poisson sampling of the number of H I absorbers in redshift intervals, Δz, from $z = 0$ to a specified redshift, $z_{\rm em}$. Following Inoue et al. (2014) we select a value of $\Delta z = 5 \times 10^{-5}$,

[1] All code for producing IGM transmission curves is open source and available at https://github.com/robbassett/TAOIST_M C.

noting, however, that deviations from this value would not affect our results. The value of $z_{\rm em}$ for a given analysis is determined by the redshift of the galaxy, or sample of galaxies, being considered. In this work, we create suites of 10 000 IGM transmission functions at 10 discrete $z_{\rm em}$ values in the range 2.9–3.9 with $\Delta z_{\rm em} = 0.1$ (we also explore IGM transmission bias at $z = 2.4$ and $z = 4.4$ for *HST* F275W and F435W observations, respectively, in Section 4.5).

To generate a single $T_{\rm IGM}$ function at a given $z_{\rm em}$, we must first produce a random sampling of hydrogen absorption systems in redshift bins of $\Delta z = 5 \times 10^{-5}$ from $z = 0$ to $z_{\rm em}$. This is achieved assuming a differential H I column density distribution, $f(N_{\rm H\,I}, X)$, following the prescriptions outlined for the 'IGM+CGM' model in S18 Appendix B. In each redshift interval, we derive the expected number of absorption systems in each bin of $\log(N_{\rm H\,I})$ (sampled from $\log(N_{\rm H\,I}) = 12.0$–$21.0$ with $\Delta\log(N_{\rm H\,I}) = 0.1$) as

$$N_{\rm abs} = \int_{N_{\rm H\,I,min}}^{N_{\rm H\,I,max}} \int_{z}^{z+\Delta z} N_{\rm H\,I}^{-\beta} A(1+z)^{\gamma} {\rm d}N_{\rm H\,I}{\rm d}z, \quad (1)$$

where $N_{\rm H\,I,min}$ and $N_{\rm H\,I,max}$ are the lower and upper bounds, β is the slope of $f(N_{\rm H\,I}, X)$, A is a constant chosen to match observed $N_{\rm abs}$, and γ describes the redshift evolution of $N_{\rm abs}$. Values for β, A, and γ are taken directly from table B1 of S18. We assume the presence of absorption systems is a Poissonian process, thus for each sightline the number of absorption systems at a given z and $N_{\rm H\,I}$ is calculated using NUMPY.RANDOM.POISSON with λ set to $N_{\rm abs}$.

For each individual absorber in a given observed sightline, we then apply the transmission function for LyC photons at $\lambda_{\rm rest} \leq 911.8$ Å and a transmission for Lyman series forest for photons with $\lambda_{\rm rest} \geq 911.8$ Å, noting that in this case we are considering the rest wavelength at the redshift of the absorption system and *not* the LyC-emitting galaxy. For LyC photons, we apply the functional form:

$$\tau_{\rm H\,I}^{\rm LyC}(\nu_{\rm rest}) = N_{\rm H\,I}\sigma_{\rm H\,I}(\nu_{\rm rest}), \quad (2)$$

where $\nu_{\rm rest}$ is the photon frequency at the rest frame of a given absorbtion system and $\sigma_{\rm H\,I}(\nu_{\rm rest})$ is the frequency-dependent interaction cross-section of H I to ionizing photons given by $\sigma_L(\nu_{\rm rest}/\nu_{911.8\text{Å}})^{-3}$. Here, σ_L is a constant with a value of 6.3×10^{-18} cm^2 (Osterbrock 1989). For Lyman series lines, we use the following for each Lyman transition, i (e.g. Inoue & Iwata 2008)

$$\tau_i(\nu_{\rm rest}) = N_{\rm H\,I}\frac{\sqrt{\pi}e^2 f_i}{m_{\rm e}c\nu_{\rm D}}\phi_i(\nu_{\rm rest}), \quad (3)$$

where $m_{\rm e}$ and e are the electron mass and charge, respectively, and c is the speed of light. The parameter f_i is the oscillator strength of Lyman transition i, which we take from tables provided with the VPFIT package (Carswell & Webb 2014). In our calculation, we include the first 32 Lyman series transitions. $\nu_{\rm D} = \nu_i(b/c)$ is the Doppler broadening of the Lyman line at frequency ν_i where b, the Doppler parameter, is randomly sampled from (Hui & Rutledge 1999)

$$h(b) = \frac{4b_\sigma^4}{b^5}e^{-b_\sigma^4/b^4} \quad (4)$$

with $b_\sigma = 23$ km s^{-1} (e.g. Janknecht et al. 2006). Finally, $\phi_i(\nu)$, the absorption profile, is taken as the analytic approximation of the Voigt profile given by Tepper-García (2006). Here, as with f_i, we also sample Γ_i, the damping constant for transition i, from the VPFIT values. The total optical depth of an individual absorber is then taken as $\tau(\nu) = \tau_{\rm H\,I}^{LyC}(\nu_{\rm rest}) + \Sigma\tau_i(\nu_{\rm rest})$, where ν refers to the observed frame frequency, $\nu = \nu_{\rm rest}/(1+z)$. The total $\tau(\nu)$ for a given sightline is the sum of the ensemble of $\tau(\nu)$ for all absorbers in that sightline.

It is worth mentioning that our transmission curves are produced as a function of wavelength, rather than frequency, and we employ a fixed resolution of $\Delta\lambda = 2.2$ Å per pixel in the observed frame. This choice is motivated by the fact that we compare extensively with LRIS spectroscopy of S18, who quote a spectral resolution of 2.18 Å per pixel for their observations. Inoue & Iwata (2008) note that spectral resolution can have a significant impact on the resultant IGM transmission, we have tested the effect of increasing the spectral resolution to 0.4 Å per pixel, finding no statistically significant difference compared to our standard 2.2 Å per pixel transmission curves.

Throughout this paper, we consider values in terms of IGM transmission, $T_{\rm IGM} = e^{-\tau}$, rather than considering τ computed as described above. The reasons being first that the value of $T_{\rm IGM}$ is typically included in calculations of $f_{\rm esc}$ and second that $T_{\rm IGM}$ has a dynamic range between 0 and 1, which provides more intuitive comparisons. We note that throughout this paper the symbol $T_{\rm IGM}$ may refer to a wavelength dependent transmission function or a single value at some specified wavelength. We avoid introducing an explicitly wavelength dependent symbol, i.e. $T_{\rm IGM}(\lambda)$, as the usage here is consistent with the conventions in the literature (e.g. Inoue & Iwata 2008).

Example IGM transmission functions at $z = 3.1$ are shown in Fig. 1. In the left-hand panel, in black we show the mean transmission curve of all 10 000 simulated sightlines at $z = 3.1$, while the gold and cyan curves show two individual sightlines having the highest and lowest $\lambda_{\rm rest} = 910$ Å transmission, respectively. At a given redshift, the transmission of LyC in the IGM may vary from 0.0 to nearly 1.0. In the right-hand panel, we show the redshift evolution of the mean Ly α and LyC transmission predicted by TAOIST-MC in comparison with observational and theoretical estimates from the literature. In all cases, our model agrees, within errors, with previously reported results.

We note that our measurements are systematically lower than some previous results, which can be attributed to the inclusion of the circumgalactic medium component introduced in S18. Furthermore, a single statistic (such as the mean) belies the complexity of the underlying $T_{\rm IGM}$ distribution as shown in Fig. 2. Thus, we do not place a large emphasis on differences between the average values of $T_{\rm IGM}$ between different studies. For theoretical $T_{\rm IGM}$ functions, this behaviour may be, in part, attributed to the exact form of the differential $N_{\rm H\,I}$ distribution assumed and the details of the implementation. For example, Inoue & Iwata (2008) and S18 assume different behaviours for the exponent β of $f(N_{\rm H\,I}, X)$ producing different relative numbers of low and high $N_{\rm H\,I}$ systems. These differences will affect the $T_{\rm IGM}$ of LyC and Ly α differently and will appear as complex systematic offsets between the mean $T_{\rm IGM}$ at a given redshift between the two implementations. It should also be mentioned that, to our knowledge, no study employing MC simulations of IGM transmission curves have accounted for the effects of H I clustering, which may further alter the mean $T_{\rm IGM}$ curve (see, however, Kakiichi & Dijkstra 2018, who demonstrate Ly α may be more attenuated from galaxies in high-density environments).

Differences in the behaviour between theoretical $T_{\rm IGM}$ implementations are only apparent from the mean transmission curves, while individual IGM transmission curves are likely indistinguishable. The implications regarding the statistical behaviour of IGM sightline ensembles, however, is precisely the topic of this paper. As we will repeat, the absolute values of quantities calculated throughout will be imprinted with the assumptions regarding our $N_{\rm H\,I}$ distribution sampling and may change slightly if different implementations are used. Thus, it is key to keep in mind that the absolute results are

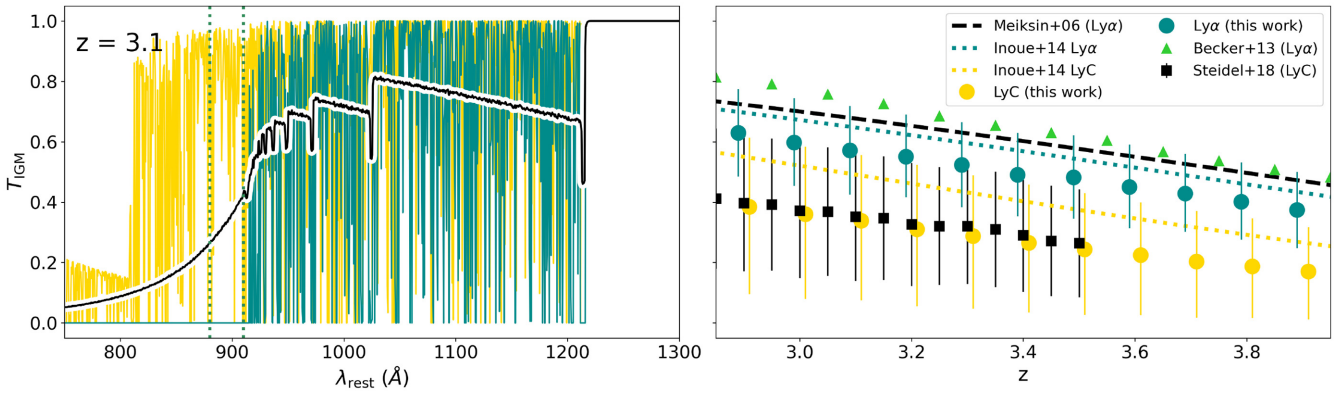

Figure 1. *Left:* Example IGM transmission function for a galaxy at $z = 3.1$. In gold and cyan are single transmission functions with highest and lowest T_{IGM} at $880 < \lambda < 910$ Å (range indicated by the vertical, cyan, dotted lines) among our ensemble of 10 000 transmission functions at $z = 3.1$. The black curve shows the average transmission for the entire ensemble. *Right:* The mean transmission of Ly α ($1210 < \lambda < 1215$ Å, cyan) and LyC emission ($880 < \lambda < 910$ Å, gold) as a function of redshift for our simulated IGM transmission functions. The error bars indicate the range containing 68.1 per cent of all values about the median in each bin. We note that mean and median values differ given the complex, bimodal underlying distribution. Here, we also compare to theoretical and observational work in the literature from Becker et al. (2013), Meiksin (2006), Inoue et al. (2014), and S18.

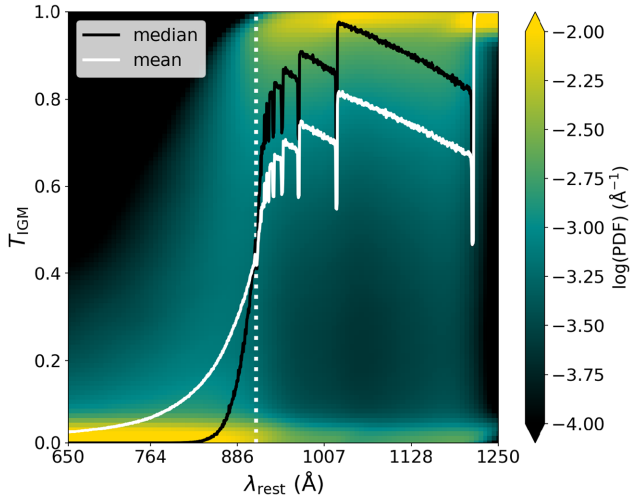

Figure 2. A full statistical description of our 10 000 IGM transmission functions at $z = 3.1$. The shading represents the probability of a given T_{IGM} value at each wavelength with probability increasing from black to gold (note the colour scaling is logarithmic). Blueward of the Lyman limit (911.8 Å, the white-dotted line) T_{IGM} is strongly peaked at $T_{IGM} = 0$. The behaviour at fixed λ shifts from unimodal at the shortest wavelengths to bimodal redwards of ∼880 Å. For illustration, we show the median and mean T_{IGM} functions in black and cyan.

for our implementation only. Qualitatively, however, our results are independent of the various input parameters.

2.2 f_{esc} distribution functions

One of the key unknowns in this study is the distribution function of f_{esc} for galaxies at $z \geq 2.9$. While quantifying f_{esc} from galaxies has been a long-standing goal in the astrophysics of reionization, this parameter remains elusive. In a broad sense, a number of studies have estimated the average f_{esc} required for all galaxies in order to match the constraints on the timing of reionization, finding values in the range $0.05 < \langle f_{esc} \rangle < 0.20$ (e.g. Bouwens et al. 2015; Robertson et al. 2015; Finkelstein et al. 2019). From hydrodynamical simulations of individual galaxies employing full radiative transfer, however, the likelihood that all galaxies will have a constant and/or single valued f_{esc} over their lifetime seems vanishingly small (Kimm & Cen 2014; Paardekooper et al. 2015, see also Section 4.6 for a brief discussion of the 3D versus line-of-sight f_{esc} values).

Given the lack of strong constraints on f_{esc} from the literature, for the fiducial model of our analysis, presented in Section 3.1, we simply uniformly apply values of f_{esc} between 0.0 and 1.0 to our mock spectra. This allows for mock spectra with the highest possible LyC flux for a given IGM sightline, representing the most likely galaxies to be detected in a LyC survey. As such, the results of our fiducial model should be interpreted as the *minimum* level of T_{IGM} bias expected for LyC-detected galaxies.

It seems most likely that allowing extremely high f_{esc} is unrealistic for the vast majority of real galaxies (e.g. Vanzella et al. 2010; Siana et al. 2015; Japelj et al. 2017). In Section 3.2, we test the effects on our measured T_{IGM} bias of applying an additional, more realistic f_{esc} distribution, to our simulations. For this test, we assume an exponentially declining f_{esc} PDF, i.e. $P(f_{esc}) \propto e^{-1/\eta}$, resulting in a model with the most probable value of f_{esc} being zero. For our exponentially declining f_{esc} PDF, we choose a value of $\eta = 0.5$, which is motivated by the observed detection rates of KLCS (S18, see Section 4.3). We illustrate the relative PDF shapes of our fiducial and exponentially declining models in Fig. 3 for clarity.

2.3 Producing mock galaxy spectra

As mentioned above, the process of producing mock galaxy spectra for our simulations requires three inputs: an underlying SED model, an IGM attenuation function, and a value for f_{esc}(LyC). We note that in much of this work we ignore the effects of dust attenuation (see, however, Section 4.4, simply noting that most LyC detections appear to originate from relatively dust-free galaxies (e.g. S18). Similar to S18, we construct our SEDs from the BPASSv2.1 (Eldridge et al. 2017) models with $Z_* = 0.001$, IMF slope $\alpha = -2.35$, and stellar mass limit of 300 $M_\odot$. We employ a model with an exponentially declining SFR with an e-folding time of 0.1 Gyr sampled at an age of ∼200 Myr. This provides an input spectrum with an intrinsic LyC to UV flux ratio, $(L_{900}/L_{1500})_{int}$, of 0.18 (e.g. S18). Our SED model corresponds to a LyC photon production efficiency, ξ_{ion}, of $\log_{10}(\xi_{ion}) = 25.61$ Hz erg^{-1}, consistent with

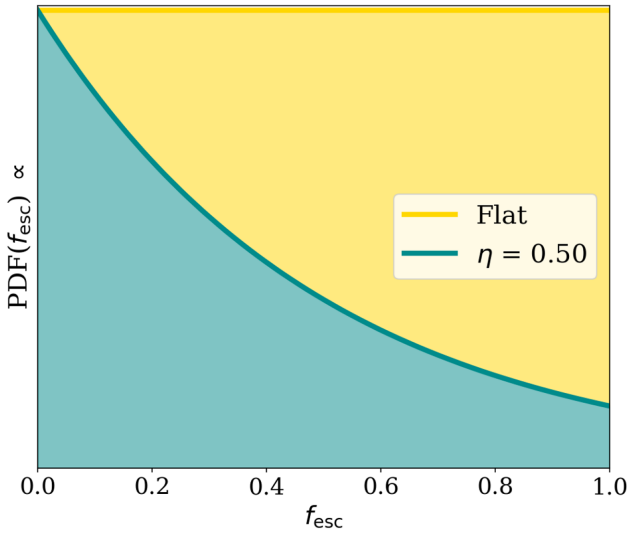

Figure 3. A comparison of the two f_{esc} PDFs used in this work. The 'Flat' distribution represents the case of no assumed prior when calculating f_{esc} and is representative of most studies in the literature. The alternative explored here is an exponentially declining models of the form PDF $\propto e^{-1/\eta}$, here shown with $\eta = 0.50$.

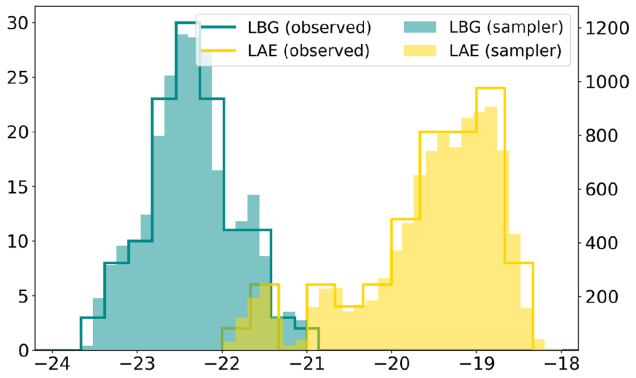

Figure 4. Input 1500 Å absolute magnitude distributions for LBG (cyan) and LAE (gold) samples. The open histograms represent LRIS 1500 Å fluxes from S18 and UV magnitudes from ground-based imaging reported in F19 for LBGs and LAEs, respectively. The filled histograms represent one realization of 10 000 sampled values for our mock galaxy spectra produced using CDF_SAMPLER.PY (see footnote 2) with the open histograms as inputs. Values on the left *y*-axis refer to observed samples (the open histograms) and on the right *y*-axis refer to mock samples (the closed histograms), noting in the latter case these values are based on an arbitrarily selected 'parent sample' size.

estimates for high redshift star-forming galaxies (e.g. Bouwens et al. 2016). We explore the effect of altering $(L_{900}/L_{1500})_{int}$ on our results in Section 3.3.

Each mock spectrum is scaled such that the non-ionizing UV flux matches a randomly sampled value characteristic of high redshift, highly star-forming galaxies. The sampling of UV fluxes is one key factor in our analysis as this ultimately determines the intrinsic level of LyC flux from galaxies in our mock samples. In this work, we test samples taken two different UV flux distributions: one based on the full sample of galaxies observed by the KLCS, which is composed of a representative subsample of bright Lyman Break Galaxies (LBGs) at $2.9 < z < 3.2$ from the flux-limited sample of Reddy et al. (2012), and a second based on $z \sim 3.1$, narrow-band selected Ly α emitters (LAEs) characteristic of galaxies targeted by LACES (F19). For our LBG comparison, UV values used in our work are sampled from measurements of LRIS spectra at $\lambda_{rest} = 1500$ Å taken directly from reported values of S18. For the comparison with LAEs, UV values are sampled based on the histograms presented in F19, fig. 15, based on ground-based photometry. We compare the absolute magnitude distributions of the two distributions in Fig. 4, showing LAEs to be significantly fainter than LBGs.[2] We note, however, that some LBGs have been shown to also exhibit Ly α emission (e.g. Shapley et al. 2003), thus LBG and LAE classifications are based on selection methodology. Here, the important distinction is the relative non-ionizing UV flux with LBGs being significantly brighter.

The sample of S18 covers a redshift range of $z \simeq 2.8-3.5$ and the sample of F19 is at a roughly fixed redshift of 3.1. The mock galaxies in our analysis, however, are produced at 10 discrete redshift values with $\Delta z = 0.1$ from $z = 2.9$ to $z = 3.9$. Thus, we must include a method to account for cosmological dimming of each of these samples when considering higher redshifts. In each case, we begin with the absolute magnitude distributions shown in Fig. 4 and assume that this distribution is roughly representative of a similarly selected sample in each $\Delta z = 0.1$ redshift bin. We then sample magnitudes from the above distributions then convert each value to an observed 1500 Å flux at a given redshift. We note that this is equivalent to a slight increase in depth with redshift, however, we expect this to have a negligible effect on our results as we are most sensitive to the brightest galaxies at any redshift.

For each of the 10 000 IGM sightlines in a given redshift bin, we produce 100 mock spectra for both the LBG and LAE comparison samples. For each trial, we randomly sample a 1500 Å flux (as described above) and a value of f_{esc}, the latter following Section 2.2. The current T_{IGM} function is applied to the input BPASSv2.1 spectrum, then at all wavelengths shortward of 911.8 Å it is scaled uniformly by the randomly selected f_{esc} value. The resulting spectrum is then scaled to match the randomly selected 1500 Å flux. Thus, in each redshift bin we produce one million galaxy spectra ensuring that the 1500 Å flux and f_{esc} distributions are well sampled. Example spectra can be seen in Fig. 5.

We can summarize the construction of each individual mock spectrum with the following equation:

$$F_{\nu}^{i,j}(\lambda, z) = F_{\nu,\mathrm{mod}}(\lambda)\frac{F_{1500,\mathrm{obs}}^{i}}{F_{1500,\mathrm{mod}}}T_{\mathrm{IGM}}^{j}(\lambda)f_{\mathrm{esc}}^{i}(\lambda), \quad (5)$$

where $F_{\nu,\mathrm{mod}}(\lambda, z)$ is the input BPASS spectrum, $F_{1500,obs}^{i}$ is the ith randomly sampled 1500 Å flux (noting again that here we have included cosmological dimming), $F_{1500,\mathrm{mod}}$ is the 1500 Å flux of the BPASS model (taken as the mean value at $1450 < \lambda < 1550$ Å), T_{IGM}^{j} is the current IGM transmission curve (we use the superscript j to indicate that the same IGM transmission curve will be used 100 times, thus it is not unique to mock spectrum i), and $f_{\mathrm{esc}}^{i}(\lambda)$ is a step function representation of the ith randomly sampled f_{esc} value given as

$$f_{\mathrm{esc}}^{i}(\lambda) = \begin{cases} f_{\mathrm{esc}}^{i} & \text{if } \lambda < 911.8 \\ 1 & \text{if } \lambda \geq 911.8 \end{cases}. \quad (6)$$

[2]In both cases, sampling of UV fluxes is achieved using the HISTOGRAM_OVERSAMPLER class of the code CDF_SAMPLER.PY (https://github.com/robbassett/cdf_sampler) with spline fitting enabled to remove sharp edges of the histogram bins.

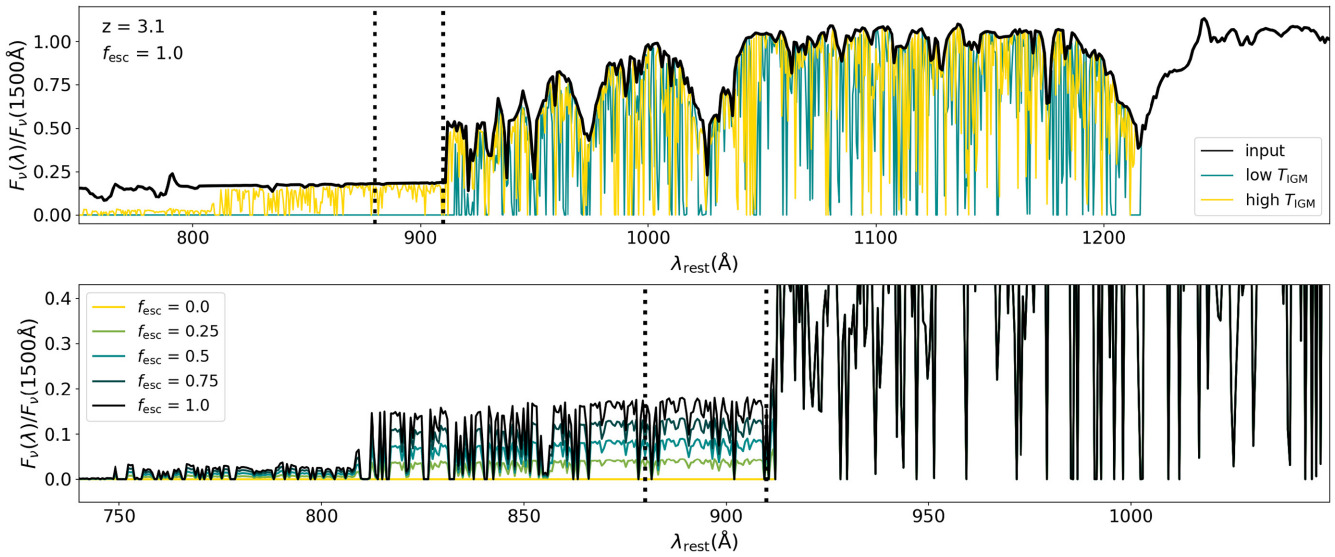

Figure 5. *Top:* Example BPASSv2.1 spectra used in this study. In black is shown the input spectrum and in gold and cyan we show the output spectra with the high and low IGM transmission curves shown in Fig. 1. In this panel, both spectra are shown for the $f_{esc} = 1.0$ case. *Bottom:* The effect of our flat treatment of f_{esc} on the output spectra for the high IGM transmission spectrum shown in the top panel with f_{esc} varying from 0.0 to 1.0. For all spectra in both panels, we show the flux in F_ν normalized to the flux at a rest wavelength of 1500 Å.

3 RESULTS

The primary results of this paper concern quantifying the observational bias in IGM transmission for samples of LyC-detected galaxies. We reiterate that the initial results are based on tests performed on a fiducial dust-free, exponentially declining SFR SED models at fixed metallicity, IMF slope, and age (see Section 2.3 for a full description). We have selected our fiducial model to have $(L_{900}/L_{1500})_{int} \sim 0.18$ (comparable to other studies in the literature, e.g. S18, F19), which is expected to be representative of young, star-forming galaxies responsible for driving reionization.

Additionally, as described in Section 2.2, our fiducial model assumes the unrealistic case of a flat probability distribution for f_{esc} between 0 and 1.0. High f_{esc} will correspond to a bright LyC flux, thus, we expect a preference towards detections at high f_{esc} in our fiducial model. f_{esc} for real galaxies will be, on average, lower than the average of our fiducial model given the typically low value for observed LyC emitters (e.g. S18). This means that the level of bias in T_{IGM} for detections seen in our fiducial model can be seen as a lower limit to the true bias for observed galaxy samples.

We explore the quantitative effects of both altering the input PDF of f_{esc} and changing the value of $(L_{900}/L_{1500})_{int}$ in Sections 3.2 and 3.3, respectively. In the case of SED variations, we test SEDs with ξ_{ion} values covering the range for exponentially declining SFR models using BPASSv2.1 spectra over available range of stellar population ages provided.

3.1 Fiducial IGM bias

Here, we quantify the bias in T_{IGM} affecting samples of LyC-detected galaxies when compared with the average T_{IGM} of all random sightlines. Formally, we define this bias as

$$T_{bias} = \langle T_{det} \rangle - \langle T_{IGM} \rangle, \quad (7)$$

where $\langle T_{det} \rangle$ is the average T_{IGM} for galaxies with LyC detected above a specified detection limit and $\langle T_{IGM} \rangle$ is the average T_{IGM} for all sightlines. It is worth noting that transmission values are not inherently additive quantities and it could be argued that the definition $T_{bias} = \langle T_{det} \rangle / \langle T_{IGM} \rangle$ is more sensible, and possibly more physically motivated as it relates directly to a difference in optical depth/H I column density. Our choice of definition is motivated by the fact that the resulting T_{bias} values are roughly redshift independent at fixed observational detection limit (see e.g. Section 3.1.3), providing a simplified framework for applying T_{bias} to a given set of observations. We also point out that, by definition, such a correction will never result in an unphysical transmission value for LyC detections > 1.0. Furthermore, any evolution in T_{bias} with redshift when assuming a fractional definition is primarily reflective of the redshift evolution of $\langle T_{IGM} \rangle$ as one is dividing by a value increasingly close to zero. Regardless, either T_{bias} definition mentioned here will provide an equivalent correction, thus the choice is somewhat arbitrary.

In this work, the calculation of T_{bias} is performed at 11 discrete redshifts in the range $2.9 \leq z \leq 3.9$ with $\Delta z = 0.1$. We also note that, similar to T_{IGM} and $\langle T_{IGM} \rangle$, T_{bias} can refer to a wavelength dependent function, a single value at a specified wavelength, or an average value across a specified wavelength range. Due to technical differences between LyC searches employing spectroscopy (e.g. S18) and photometry (F19, M20), we present the two cases separately: spectroscopic biases are presented in Section 3.1.1 and photometric biases are presented in Section 3.1.2. In all cases, we have performed this experiment twice: once for an LBG-like sample and once for a fainter, LAE-like sample (see Fig. 4). Due to the inherent faintness, our mock LAE samples are typically only detected deep *HST* F336W observations, which compare to F19 (particularly in our higher redshift bins) who achieve a depth of 30.24 mag. Thus, in most cases we only provide T_{bias} measurements for this comparison (as opposed to spectroscopy or CFHT u photometry). We provide a summary of our fiducial model in Section 3.1.3.

3.1.1 *Spectroscopic detections*

Spectroscopic detection of LyC radiation provides a key advantage over photometric detections in terms of interpretation in the context

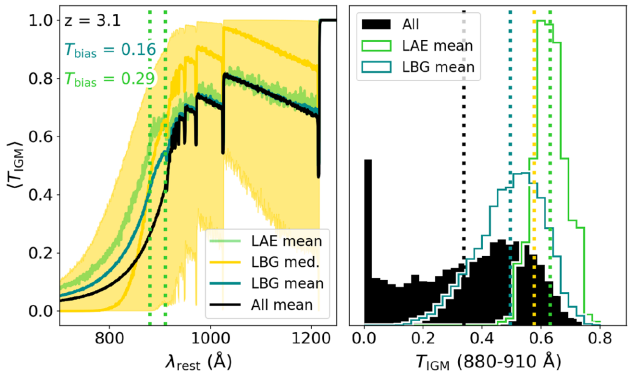

Figure 6. *Left column:* $\langle T_{IGM} \rangle$ for spectroscopically detected LyC emission. Shown are results at $z = 3.1$, similar to the average redshift of S18 of ∼3.05. The Lyman limit is indicated with a vertical dotted line, and in all cases the detection limit is fixed at 0.025 μJy (∼27.9 mag), equivalent to a 1–5σ detection, dependent on individual targets, in the sample of S18. The mean and median $\langle T_{IGM} \rangle$ functions for detected LBG-like galaxies are shown with the cyan and gold lines with the gold-shaded area enclosing 68 per cent of T_{IGM} values for detected galaxies at a given wavelength. Thus, the lower bound of the gold-shaded region is not representative of the transmission curve shape for any individual sightline. $\langle T_{IGM} \rangle$ for LyC detected, LAE-like galaxies is shown in green, significantly higher than for the LBG-like sample due to their relative faintness. The increased dispersion seen for LAE samples is a result of a smaller number of detections for such galaxies. The mean T_{IGM} for all sightlines is shown in black for comparison. *Right column:* Normalized histograms of T_{IGM} for all sightlines (black), detected, LBG-like galaxies (cyan), and detected, LAE-like galaxies (green). The mean for all galaxies and detections is shown with the corresponding vertical, dotted lines (matched to the corresponding open histograms), and the median for LBG-like detections is shown with a gold-dotted line, noting that this line corresponds to the gold line of the left-hand panel and has no matching histogram in the right-hand panel.

of estimating f_{esc}. The reason being that spectroscopy allows one to probe the same *rest frame* wavelengths just shortwards of the Lyman limit, typically probed between 880 and 910 Å, independent of redshift in theory. In practice, of course, the redshift range in which LyC can be probed by a given set of spectroscopic observations is defined by the wavelength coverage of the instrument used. Furthermore, the detection limits of a given instrument will be wavelength dependent due to response variations of the detector. Thus, the experiment presented here should be considered as a simulation of an idealized spectroscopic instrument with uniform sensitivity to LyC radiation at 880–910 Å across the entire redshift interval from $2.9 < z < 3.9$. The black $\langle T_{IGM} \rangle$ functions in Fig. 6 show that this wavelength range exhibits the largest $\langle T_{IGM} \rangle$ values at $\lambda_{rest} < 911.8$ Å meaning that at all redshifts spectroscopic observations probe LyC emission at the highest $\langle T_{IGM} \rangle$ and, thus, the highest probability of detection (at fixed depth). This is simply due to the fact that the redshift interval of LyC absorption systems that affect a given wavelength increases with decreasing wavelength. This means that at lower wavelengths the probability of encountering a high column density system in any individual sightline is higher.

As we discuss later, this is not the case for photometric observations that instead probe a fixed λ_{obs} range, thus a decreasing λ_{rest} with increasing redshift. Another important and related point is that ionizing radiation escaping from galaxies will be completely absorbed by intervening, high H I column density systems, resulting in rapid drops in flux based on the redshift of that intervening system (e.g. the drop at ∼810 Å in Fig. 1). This means that escaping ionizing radiation from high-redshift galaxies may only be visible in a very small wavelength range and this behaviour will be difficult to capture and interpret from photometric observations, but will be seen clearly in spectroscopy. As a caveat, however, we note that, without ancillary, high spatial resolution, space-based photometric data, it can be difficult to rule out the possibility of low-redshift contamination from ground-based spectroscopic LyC detections (Vanzella et al. 2010, 2012).

The fact that spectroscopy probes the most transparent portion of the emitted spectrum from high-redshift galaxies also suggests that spectroscopic detections of LyC may suffer from relatively low T_{bias} at fixed detection limits (noting, however, that photometric detections are significantly deeper for the same exposure time). We show this in Fig. 6 where we show $\langle T_{IGM} \rangle$ for all 10 000 sightlines in black and $\langle T_{IGM} \rangle$ for those where galaxies are detected with a flux above 0.025 μJy, equivalent to ∼27.9 mag, at $z = 3.1$, with coloured lines. It should be clarified here that this detection limit is chosen to be roughly matched to the faintest LyC detection reported in S18 for the galaxy Westphal-MM37 (0.026μJy). Considering the full parent sample of S18, 0.025 μJy corresponds to a 1–5σ detection as the observational limits and noise characteristics exhibit complex dependencies on factors such as observational depth and source redshift (i.e. the observed wavelength of emitted LyC radiation). Thus, we reiterate that our results are representative of an idealized version of the S18 survey as we have not attempted to simulate the full complexity of their spectroscopic observations.

Returning to Fig. 6, the cyan and gold lines indicate the mean and median T_{IGM} curves for LyC-detected, LBG-like galaxies (comparable to the S18 sample), while the green line shows the mean T_{IGM} curve for LAE-like detections (comparable to the F19 sample). Here, we measure $\langle T_{IGM} \rangle$ in the rest frame wavelength range $880 \leq \lambda_{rest} \leq 910$ Å (indicated in Fig. 6), also following S18. We note that LAE-like galaxies are not representative of the S18 sample and are only detected at these spectroscopic limits in our lowest redshift bins. In fact, overall detection rates at all redshifts is lower for the more faint sample of LAEs, which accounts for the increased dispersion seen in the $\langle T_{det} \rangle$ curve for LyC-detected LAEs. Given this comparison is to S18 who focus on LBGs, we do not place a large emphasis on this mock sample for spectroscopic observations.

Also shown in Fig. 6 is the median and 68 percentile range for LyC-detected LBGs in gold for comparison. The median value of T_{IGM} for detections is seen to be larger in the Ly α forest and lower beyond the Lyman limit, with a cross-over value around 880 Å. The significant differences between the mean and median IGM transmission functions for detected galaxies is a reflection of the non-Gaussian nature of the underlying T_{IGM} distribution (see Fig. 2). Regardless, the median and mean values of T_{IGM} for detected galaxies are similar and throughout the remainder of this work we focus on the mean value.

In the right-hand column of Fig. 6, we compare the histograms of T_{IGM} at 880–910 Å between all sightlines (black) and those associated with LBG-like galaxies detected above 0.025 μJy (cyan). We can see that the underlying distribution is bimodal with the most probable value of T_{IGM} being ∼0, while the distribution for detections is unimodal with the most probable value being close to the upper mode of the underlying distribution (the distribution for fainter, LAE-like samples, shown in green, is skewed towards even higher values). This is not surprising as for galaxy to be detected at LyC wavelengths the value of T_{IGM} must not be zero. It is clear that the mean value of T_{IGM} for all sightlines falls between the peaks of the underlying T_{IGM} distributions and is thus not among the most probably values for detected galaxies.

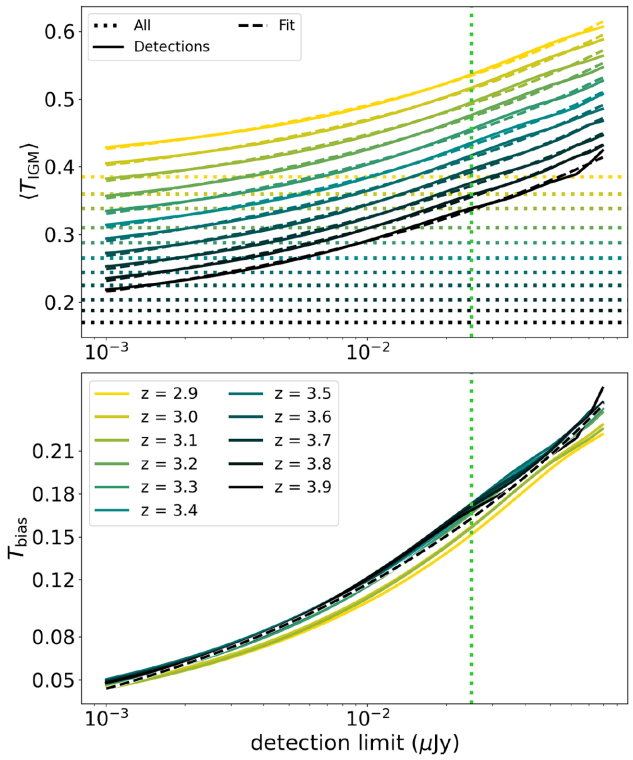

Figure 7. The dependence of $T_{\rm bias}$ on the detection limit of spectroscopic observations ($F_{\rm lim}$) for LBG-like detections. *Top:* $\langle T_{\rm IGM}\rangle$ as a function of $F_{\rm lim}$ at redshifts between 2.9 and 3.9 (see lower panel for legend). The horizontal dotted lines show $\langle T_{\rm IGM}\rangle$ of all sightlines at a given redshift, and the vertical dotted line shows the $F_{\rm lim}$ assumed in Fig. 6. At each redshift, we fit the curve of $\langle T_{\rm IGM}\rangle$ for detected galaxies with a power law of the form $\langle T_{\rm IGM}\rangle(F_{\rm lim}) = aF_{\rm lim}^{k} + \epsilon$. *Bottom:* $T_{\rm bias}$ as a function of $F_{\rm lim}$ for the same redshift interval. We show a power-law fit, $T_{\rm bias}(F_{\rm lim}) = aF_{\rm lim}^{k} + \epsilon$, to the combined data for all redshifts as a black-dashed line.

The fact that LyC detections cannot occur at $T_{\rm IGM} = 0$ may occasionally be overlooked in calculations of $f_{\rm esc}$ for LyC-detected galaxies, and is key to the narrative of this work. Careful consideration of $T_{\rm IGM}$ variation in the estimate of $f_{\rm esc}$ for individual detections is common practice (e.g. Shapley et al. 2006; Inoue et al. 2011; Vanzella et al. 2016). Ultimately, the goal of this paper is to provide a clear quantification of this effect. A primary application of our results will be for estimating $\langle f_{\rm esc}\rangle$ for larger samples of LyC-detected galaxies that may be returned by future, extremely deep surveys (see Section 5). It should also be mentioned that, when estimating upper limits in $f_{\rm esc}$ for samples including LyC non-detections, $\langle T_{\rm IGM}\rangle$ considering all simulated sightlines is appropriate (i.e. inclusion of $T_{\rm bias}$ is unnecessary).

The level of $T_{\rm bias}$ for LyC detections will also be sensitive to the detection limits, $F_{\rm lim}$, of a given set of observations. We explore the dependence between $T_{\rm bias}$ and spectroscopic detection limits in Fig. 7. In the top panel of Fig. 7, we show the value of $\langle T_{\rm IGM}\rangle$ for galaxies with spectroscopically detected LyC emission as a function of detection limit at redshifts in the range $2.9 \leq z \leq 3.9$. For each redshift, we also show the corresponding $\langle T_{\rm IGM}\rangle$ for all sightlines with a dotted line of the same colour. The detection limit assumed in Fig. 7 of 0.025 μJy is shown with a green, vertical, dotted line. We find that at low detection limits the dependence between $\langle T_{\rm IGM}\rangle$ and $F_{\rm lim}$ is similar in all redshift bins apart from the expected vertical offsets due to the drop in $\langle T_{\rm IGM}\rangle$ with redshift (reiterating, however, that the definition $T_{\rm bias} = \langle T_{\rm det}\rangle/\langle T_{\rm IGM}\rangle$ will result in a clear redshift dependence). At each redshift, the curve can be well fit by a power law of the form $T_{\rm IGM} \propto F_{lim}^{\beta}$ with β in the range ∼0.26–0.35. These fits for each redshift are shown in Fig. 7 with corresponding dashed lines, noting that these relationships will change for inputs that vary from our fiducial model (e.g. different values of $(L_{900}/L_{1500})_{\rm int}$ or a different input distribution of 1500 Å fluxes). It is also worth reiterating that sensitivity variations across real spectroscopic detectors will result in detection limit variation with redshift at fixed exposure time.

In the bottom panel of Fig. 7, we show $T_{\rm bias}$ as a function of $F_{\rm lim}$ at the same discrete z values between 2.9 and 3.9 with $\Delta z = 0.1$. Overall, we find a very small scatter in $T_{\rm bias}$ with the difference between the maximum and minimum $T_{\rm bias}$ at fixed $F_{\rm lim}$ less that 0.01 at all redshifts in the range considered. Given the smooth curves seen in Fig. 7, it is tempting to provide the power-law fits (of the form $\langle T_{\rm IGM}\rangle(F_{\rm lim}) = aF_{\rm lim}^{k} + \epsilon$, the dashed lines in Fig. 7, top panel) at each redshift giving an analytical function for estimating $T_{\rm bias}$ as a function of z and $F_{\rm lim}$, however, we refrain from doing so as we would consider any application of such a function as an overinterpretation of Fig. 7, which results from our particular implementation for producing $T_{\rm IGM}$ functions as well as the various inputs of our fiducial model (e.g. here we have only shown results for LBG-like samples). For illustrative purposes, we have fit a power law to the combined $T_{\rm bias}$ versus $F_{\rm lim}$ curves $T_{\rm bias} \propto F_{\rm lim}^{0.29}$. This fit is shown in the bottom panel of Fig. 7 with a black-dashed line. Here, the choice of a power law is ad hoc, and no specific significance is assigned to the fit parameters.

It is useful here take a step back and recall two important points: first, there is significant variation in $T_{\rm IGM}$ for individual sightlines at any redshift (see e.g. Fig. 1) and secondly, the fact that we allow high $f_{\rm esc}$ values (up to 1.0) in our fiducial model meaning $T_{\rm bias}$ observed in our fiducial model represents the absolute minimum $T_{\rm bias}$ for a given detection limit. Thus, we caution the reader from applying values of $T_{\rm bias}$ calculated using a similar model to observations of *individual* galaxies when estimating $f_{\rm esc}$ without including these caveats.

3.1.2 *Photometric detections*

While spectroscopic detection of LyC radiation from galaxies provides distinct advantages in terms of $\langle T_{\rm IGM}\rangle$, achieving this for large samples of galaxies is inefficient. Photometric surveys have the potential for detecting large samples of LyC-emitting galaxies simultaneously. Another important benefit of photometric surveys when compared to spectroscopy is that photometry is significantly more sensitive (i.e. deeper) for the same exposure time. Furthermore, in the case of space-based LyC detections, ancillary data are not necessary to rule out the possibility of low-redshift contamination. Photometric LyC surveys must be performed in well-studied fields in which targeted galaxies already have accurate photometric redshift estimates (e.g. ZFOURGE fields Straatman et al. 2016) or, ideally, secure spectroscopic redshifts (e.g. 3DHST, DEIMOS10K, VANDELS, MUSE-wide; Momcheva et al. 2016; Hasinger et al. 2018; Pentericci et al. 2018; Urrutia et al. 2019). In fields such as these, specific redshift windows can be targeted using photometric bands probing LyC emission such as *HST* F336W at $z \sim 3.0$ or CFHT u at $z \sim 3.4$ (e.g. F19, M20). There are two key drawbacks in the case of photometric LyC surveys when compared to spectroscopy, however (see also S18, section 7.2).

The first drawback in photometric searches for LyC emission when compared to spectroscopic studies is that the ionizing radiation may only be observable in a narrow wavelength range just short of 912 Å

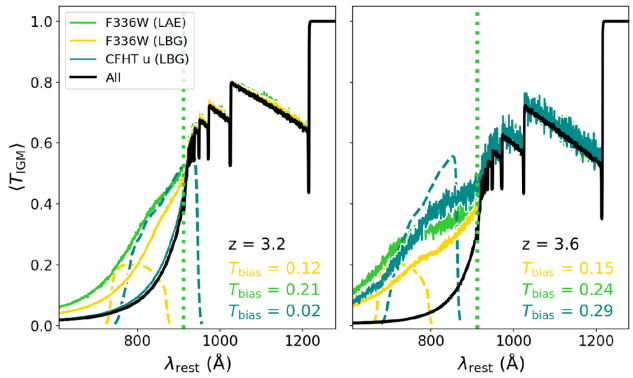

Figure 8. T_{bias} for photometrically detected LyC emission in the *HST* F336W and CFHT u filters. Results are shown at $z = 3.2$ and $z = 3.6$. F336W and CFHT u transmission curves are shown as the dashed gold and cyan lines, respectively. Detection limits are fixed at 30.24 and 27.82 mag for F336W and CFHT u, respectively (matched to F19 and M20). $\langle T_{IGM} \rangle$ for F336W and CFHT u detected LBG-like galaxies are shown in gold and cyan, respectively, and $\langle T_{IGM} \rangle$ for all sightlines is shown in black. The green line indicates $\langle T_{IGM} \rangle$ for LAE-like galaxies detected with the F336W filter, more similar to the sample of F19. The increased dispersion of the green line relative to the gold line is driven by a decrease in the total number of detected galaxies. The Lyman limit is indicated in each panel by a vertical dotted line.

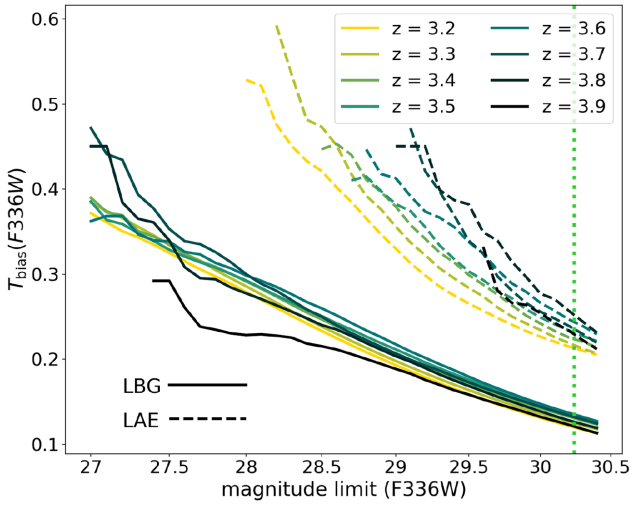

Figure 9. The dependence of T_{bias} on the detection limit of F336W observations (m_{lim}) at $3.2 \leq z \leq 3.9$ (where F336W probes LyC exclusively). Above $z = 3.2$ the level of T_{bias} is relatively constant at fixed m_{lim}. The larger redshift variation when compared to Fig. 7 and the divergent behaviour for shallow observations at high redshift reflect the shifting rest wavelengths probed by the F336W with increasing redshift.

as shown in Fig. 5. This is due to intervening, high H I column density systems at redshifts corresponding to the Lyman limit occurring at the wavelength of the drop in flux of our simulated spectra. The fact that such a drop may occur in the middle of the wavelength sensitivity of a given filter will result in an underestimation of the flux level of the emergent LyC radiation. This results from the fact that *calculation* of the reported photometric flux inherently assumes a flat flux density across the filter. Of course, the *interpretation* of the photometric flux can include more complex spectral behaviour, e.g. extreme [O III] + H β emitters presented in Forrest et al. (2017).

The second drawback is that the observed wavelengths of photometric bands are fixed. This means that the ideal redshift for such surveys is at the point where the red cut-off of the filter in question falls just below the Lyman limit (thus filter dependent). LyC radiation can be detected to higher redshifts (more likely for extremely deep observations), however, at high redshift the filter moves to bluer rest wavelengths where $\langle T_{IGM} \rangle$ is significantly lower. This fact causes significant complications when making comparisons of LyC escape from photometric detections at different redshifts. We also mention briefly here that some photometric filters suffer from so-called 'red leak' with a small amount of radiation at wavelengths longer than the optimal cut-off of the filter being transmitted (though this is minimized for the new CFHT u filter used in M20, Sawicki et al. 2019). As such features will be included in the filter curves used in our analysis, this effect is implicitly accounted for.

With these two drawbacks in mind, we present the simulated T_{bias} for LyC-detected galaxies for *HST* F336W and CFHT u detected galaxies in Fig. 8. Here, we use fixed detection limits of 30.24 and 27.82 mag for F336W and CFHT u, respectively (matched to the limits of F19 and M20). The two panels in Fig. 8 show the mean T_{IGM} for all sightlines (black), for F336W LBG-like detections (gold), CFHT u LBG-like detections (cyan), and F336W LAE-like detections (green) at redshifts of 3.2 and 3.6 (LAE-like detections for CFHT u are not shown as such detections are extremely rare due to the relative shallowness of M20 photometry). We find that T_{bias} for LBG-like galaxies is significantly lower for F336W detections, however, this is simply reflective of the greater depth of our F336W comparison rather than any intrinsic advantage of *HST* observations over ground-based for LyC detections. Comparing F336W LAE-like versus LBG-like detections, we find that T_{bias} for the former is ∼0.1 larger owing to the relative faintness of LAEs compared to LBGs (see Fig. 4).

In Fig. 8, F336W and CFHT u filters are shown with the dashed gold and cyan lines, highlighting the fact that the F336W and u filters exclusively probe LyC radiation at $z > 3.1$ and $z > 3.4$, respectively. This explains why we see a significantly lower T_{bias} for the CFHT u filter at $z = 3.2$ as the transmission of this filter peaks redward of the Lyman limit, meaning that it is more sensitive to non-ionizing radiation at this redshift. In such a case where a filter straddles the Lyman limit the interpretation of any observed flux in the context of f_{esc} is significantly complicated (e.g. Bassett et al. 2019) and such cases should be avoided where possible.

T_{bias} for photometry is also sensitive to observational detection limits. The variation in T_{bias} with detection limit (in magnitudes, m_{lim}) is demonstrated in Fig. 9 for the *HST* F336W filter. The solid lines show results for LBG-like detections and the dashed lines for LAE-like detections. Similar to spectroscopic results presented in Fig. 7, we find that, at fixed z, T_{bias} decreases linearly with an increasing magnitude limit. When compared to the spectroscopic results of Fig. 7, with $\Delta T_{bias} \lesssim 0.01$ for all redshifts, we find more variation with redshift. This is due to the changing rest-frame wavelengths probed by the F336W filter with redshift. Again, a more significant redshift evolution will be observed assuming the definition $T_{bias} = \langle T_{det} \rangle / \langle T_{IGM} \rangle$. For LAE-like detections, the fact that very few LyC fluxes reach magnitudes brighter than 28.5 (and only in the lowest redshift bins) means that detections occur in only those sightlines with the highest T_{IGM}(F336W). Thus, the trends shown for LAE samples in Fig. 9 exhibit more scatter due to an increased sensitivity to the stochasticity of our IGM transmission functions. The dashed lines in Fig. 9 also demonstrate why we find so few LyC detected LAEs for our mock spectroscopic and CFHT u observations given the depth of these two comparisons are fixed at ∼27.9 and 27.82 mag, respectively.

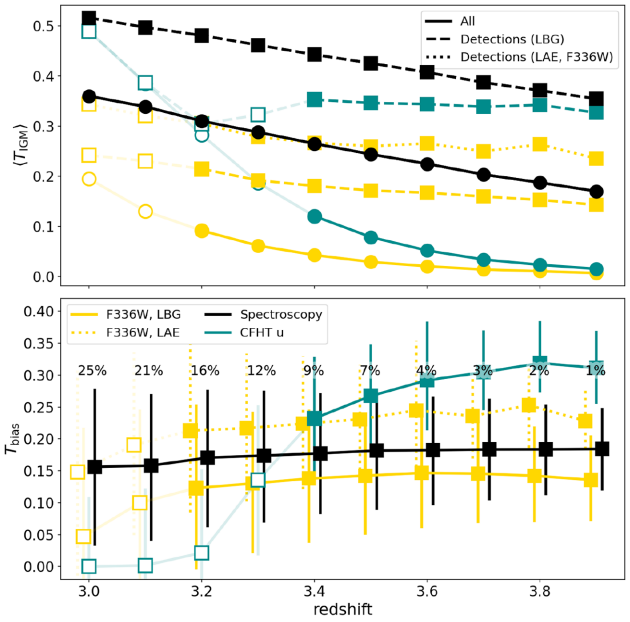

Figure 10. A summary of T_{bias} for our fiducial model. *Top:* $\langle T_{IGM} \rangle$ as a function of redshift for all sightlines are shown with the solid lines, while the dashed lines show $\langle T_{IGM} \rangle$ for detected galaxies. Results for spectroscopy, F336W, and CFHT *u* are shown in black, gold, and cyan, respectively. For our fiducial model, we assume detection limits of 0.025 μJy (∼27.9 mag), 30.24, and 27.82 mag for spectroscopy, F336W, and CFHT *u*. *Bottom:* T_{bias} as a function of redshift for each detection method. The error bars show the 68 percentile range at each redshift. Values are calculated at fixed redshifts between 3.0 and 3.9 with $\Delta z = 0.1$, slight offsets between methods are for clarity only. We also show the detection percentage for spectroscopy in black, which decreases significantly with redshift, across the top of the bottom panel. In both panels, the open symbols for photometric observations indicate redshifts at which a given filter probes (parially or entirely) wavelengths redwards of the Lyman limit (i.e. non-ionizing photons).

3.1.3 Fiducial model summary

The results of our fiducial model for fixed detection limits of 0.025 μJy (∼27.9 mag), 30.24, and 27.82 mag for spectroscopy, F336W, and CFHT *u*, respectively, are summarized in Fig. 10 for mock observations of galaxies with 1500 Å flux distributions characteristic of LBGs (F336W results for fainter, LAE-like galaxies are also shown with the dotted lines). As described in Sections 3.1.1 and 3.1.2, spectroscopic detections at this depth (targeting a fixed rest wavelength window at $880 < \lambda_{rest} < 910$ Å) experience a roughly constant T_{bias} of ∼0.15–0.17 (∼0.32 for fainter, LAE-like samples). We find a slight redshift dependence on T_{bias}, which increases from 0.157 at $z = 2.9$ to 0.173 at $z = 3.7$ then decreases slightly to 0.169 at $z = 3.9$. This change in T_{bias} of less than 2 per cent is significantly smaller than the variance seen at any given redshift and is driven entirely by our cosmological dimming (see equation 6). Thus, we conclude that T_{bias} is effectively constant at $3.0 < z < 3.9$ for our chosen definition.

The fact that T_{bias} is found to be constant with redshift is somewhat counterintuitive. Instead, one may expect a monotonic increase in T_{bias} with redshift due to the fixed detection limit and linear decrease in $\langle T_{IGM} \rangle$. For our additive definition of T_{bias}, the constant T_{bias} observed can be explained by a decrease in detection rate with redshift where only the brightest galaxies contribute to T_{bias} at the high *z* end. This is illustrated in Fig. 10 with the detection percentages for spectroscopy at each redshift indicated in black.

Condsidering photometric detections, T_{bias} is seen to increase while the Lyman limit passes through the filter in question. At redshifts where a given filter has passed fully blueward of the Lyman limit, the level of T_{bias} is seen to level off (within errors) at a value dependent on the photometric depth. For our fiducial depths, this plateau level is ∼0.11–0.14 and ∼0.22–0.31 for the F336W (magnitude limit = 30.24) and CFHT *u* filters (magnitude limit = 27.82), respectively. In the case of LAE-like 1500 Å flux distributions, we show results only for F336W as this comparison has significantly deeper flux limits compared with spectroscopy and CFHT *u* (where detections of LAE-like samples are vanishingly rare). In the case of LAEs, we find that T_{bias} is roughly 0.1 higher than for LBGs at fixed redshift, with values in the range ∼0.21–0.24 across the redshift range sampled.

We also observe a slight dip in T_{bias} for photometric detections at the highest redshifts in the bottom panel of Fig. 10. Unlike spectroscopic detections, by $z \sim 3.8$ our photometric filters are probing very blue λ_{rest} where $\langle T_{IGM} \rangle$ is near zero. Furthermore, as seen in Fig. 2, the T_{IGM} distribution at these wavelengths is a skewed, unimodal distribution peaked at $T_{IGM} = 0$. This means that the probability of finding a sightline with T_{IGM} much higher than zero is very low. This could explain why T_{bias} for photometry dips at high *z*, as even those small number of detected galaxies will be found in sightlines approaching zero transmission at wavelengths probed by a given filter. This means that the level of T_{bias} seen at lower redshifts simply cannot be maintained given the underlying T_{IGM} distribution for the wavelengths probed. At higher redshifts, the T_{IGM} distribution becomes so strongly peaked at $T_{IGM} = 0.0$ that no detections are expected, thus we do not expect the results presented here for $2.9 < z < 3.9$ to be generalizable towards higher redshifts. This is not necessarily the case for spectroscopic detections as the T_{IGM} distribution at $880 < \lambda_{rest} < 910$ Å remains bimodal even at high redshift, thus no obvious dip in T_{bias} is seen. Regardless, in all cases $\langle T_{IGM} \rangle$ is decreasing with redshift, thus detections become rarer. This manifests as a decreasing 68 percentile range for T_{bias}, a reflection of the drop in the numbers of detected galaxies with redshift.

Finally, as mentioned at the start of Section 3.1, the definition $T_{bias} = \langle T_{det} \rangle / \langle T_{IGM} \rangle$ is equally valid to the definition adopted in this work. Under this alternative definition, a very clear trend between T_{bias} and redshift is apparent increasing from ∼1.3 to ∼1.8 for spectroscopic observations and from ∼3 to ∼35 for F336W observations for LAE samples. We reiterate that, although a fractional definition may be more physical (in the sense that it relates directly to a ratio of H I column densities), the redshift evolution of T_{bias} in this case reflects primarily the fact that $\langle T_{IGM} \rangle$ moves increasingly close to zero with redshift while the actual difference in the mean IGM transmission between detections and all sightlines is roughly constant, as our chosen definition illustrates. Thus, our definition provides a simplified correction when calculating f_{esc} for LyC detected samples from an observational point of view.

3.2 An alternative f_{esc} distribution

It is expected that if LyC emission is detected from a given galaxy, it must have a high f_{esc} and/or a high T_{IGM}. From current observations of LyC emitters (particularly considering the large number of non-detections), it seems that f_{esc} values, i.e. 0.0–0.2, are most common (e.g. Boutsia et al. 2011; Grazian et al. 2016; Smith et al. 2018). The results presented for our fiducial model in Section 3.1, however, allow for f_{esc} values from 0.0 to 1.0 with no preference. This means that a large number of detections from our fiducial model exhibit

a large f_{esc} and are detected in sightlines with relatively low T_{IGM}. If we instead choose an underlying f_{esc} distribution skewed towards low f_{esc}, we might expect that the average T_{IGM} for detections will increase, thus increasing T_{bias}.

In this section, we explore how altering the PDF of selected f_{esc} values affects the level of T_{bias} and the distributions of f_{esc} for LyC detections. For comparison, the fiducial model can be treated as a flat PDF between 0 and 1. Here, we test an alternative f_{esc} PDF model designed to give more weight to lower f_{esc} values. In this case, we choose an exponentially declining f_{esc} PDF of the form

$$PDF(f_{esc}) \propto e^{-f_{esc}/\eta} \tag{8}$$

where η represents an exponential cut-off in f_{esc}. Here, we test the value $\eta = 0.50$ (see Fig. 3) motivated by LyC detection rates from S18 (see Section 4.3). For brevity, our fiducial model will be described as 'flat' and our alternative model will be referred to as $\eta = 0.50$. As with our fiducial model, for our $\eta = 0.50$ model we recreate 100 mock spectra for each of our 10 000 IGM transmission functions at each discrete redshift value as described in Section 2.3.

We show example $\langle T_{IGM} \rangle$ curves at $z = 3.1$ for detected LBG-like galaxies in each of our two models in Fig. 11. Though not shown here, results for LAE-like galaxies are qualitatively similar. Here, we see that the flat f_{esc} PDF exhibits a lower T_{bias} than the $\eta = 0.50$ as expected. The increases in T_{bias} for both spectroscopic and photometric detections are found to be only 0.01 and 0.02, respectively. These increases in T_{bias} are essentially negligible considering the spread in $\langle T_{IGM} \rangle$ for LyC detections seen in Fig. 10. Thus, in the case of our $\eta = 0.5$ model, we find no significant difference in T_{bias} when compared to the fiducial, flat f_{esc} PDF and note that this behaviour is the same in all redshift bins. In cases where the underlying f_{esc} is more strongly skewed towards $f_{esc} = 0$ (i.e. smaller values of η), the difference in T_{bias} when compared to a flat PDF is certain to increase. Such a low η model (or any other similarly skewed f_{esc} PDF) may be appropriate for galaxy samples with selection biases different from the LBG and LAE samples considered here if $\langle f_{esc} \rangle$ does indeed vary with galaxy properties (see Section 4.3 for more discussion).

The fact that T_{bias} for our $\eta = 0.5$ model is only negligibly larger than our flat f_{esc} PDF does not mean the two models are interchangeable in regards to estimates of f_{esc} from observed samples. To illustrate this, we show in Fig. 12 the histograms of f_{esc} for detections only versus all trials at $z = 3.1$ for spectroscopy (left) and F336W (right). The filled histograms show the underlying f_{esc} distributions and open histograms show the f_{esc} distribution for LyC detections. We find that the f_{esc} distributions of LyC detections (i.e. the posterior) for both observational methods is skewed towards $f_{esc} = 1.0$, inconsistent with the low values typically seen in observations. The posterior for the $\eta = 0.5$ model, on the other hand peaks at lower values, more consistent with estimates in the literature. We show the mean values for posterior distributions in each panel with a vertical dotted line. When assuming an $\eta = 0.5$ model, the inferred average f_{esc} value is lower by 0.07 and 0.12 for spectroscopy and F336W detections, respectively. Thus, although T_{bias} is roughly the same between the two f_{esc} PDF models, the differences when considering the inferred f_{esc} for galaxy samples is significant.

We note that the posterior distribution for the $\eta = 0.5$ model for a given detection method is equivalent to the posterior for the flat f_{esc} PDF model multiplied by the input $\eta = 0.5$ distribution (the prior) in line with the framework of Bayesian statistics. This is true in general, thus one can simply determine the posterior distribution for any arbitrarily defined f_{esc} PDF once the posterior for a flat distribution is determined for a given observational method and detection limit without the need to run a separate analysis. We stress again that the actual distribution of f_{esc} is essentially unknown, however, we discuss possibilities for placing some constraints on this in Sections 4.3 and 4.6.

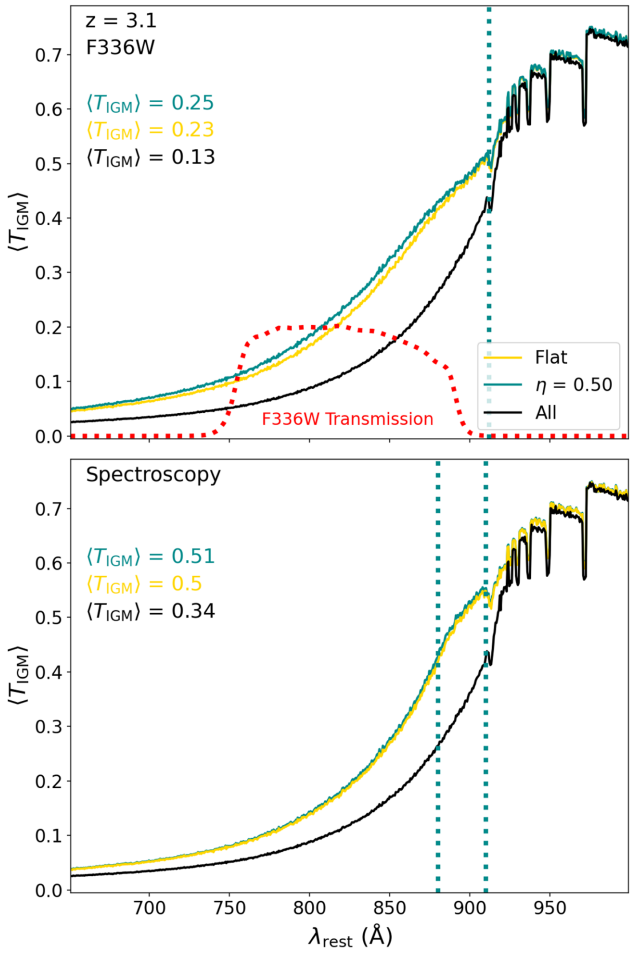

Figure 11. T_{IGM} curves for galaxies detected with F336W (top) and spectroscopically, (bottom). Both panels show the results at $z = 3.1$ with detection limits of 30.24 mag for F336W and 0.025 μJy (∼27.9 mag) for spectroscopy. In both cases, the $\eta = 0.30$ model exhibits only slightly higher T_{IGM} than the fiducial model. Spectroscopic (F336W) values of T_{bias} increase modestly from 0.16 (0.10) for the fiducial model to 0.17 (0.13) for the $\eta = 0.50$ model.

3.3 Dependence on SED variations

In this section, we briefly explore the effects that varying the SED shape will have on our estimates of T_{bias} presented in Sections 3.1 and 3.2. In regards to detecting LyC from a given galaxy above a specified limit, the key difference resulting from a change in SED shape will be a change in the flux ratio of the LyC and UV ($\lambda_{rest} \sim 1500$ Å) portions of the observed spectrum, $(F_{900}/F_{1500})_{obs}$, at a fixed T_{IGM}. The factor that will affect $(F_{900}/F_{1500})_{obs}$ (in addition to T_{IGM}) considered here is variation in the *intrinsic* ratio of LyC and UV emission, $(L_{900}/L_{1500})_{int}$.

To test the effect of altering $(L_{900}/L_{1500})_{int}$ on our results we rerun the analysis described in Section 2.3 for each age of our exponentially declining BPASSv2.1 models (with *e*-folding time-scale of 0.1 Gyr) in the range $6.0 < \log(age) < 9.0$ in steps of $\Delta\log(age) = 0.1$. The models produced exhibit $(L_{900}/L_{1500})_{int}$ in the range ∼0.07–0.77, with corresponding values of ξ_{ion} from ∼25.4–26.0. For each aged

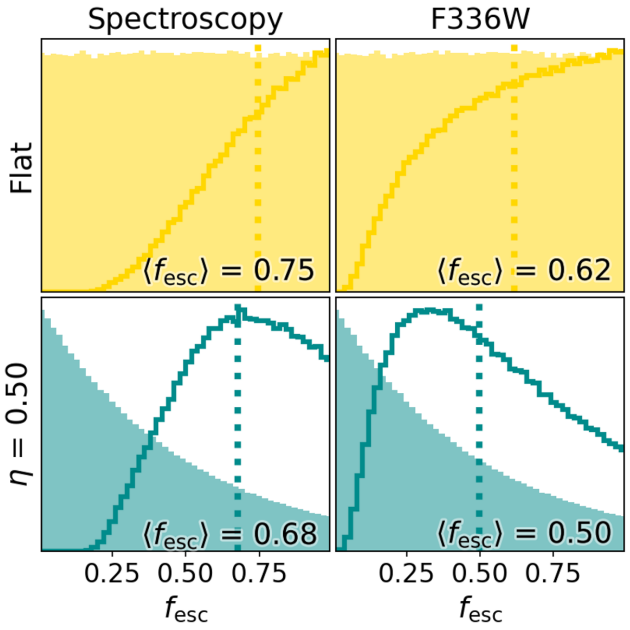

Figure 12. Histograms of f_{esc} for our two f_{esc} PDF models: flat in the top row and $\eta = 0.50$ on the bottom. The left column shows results for spectroscopy and the right for F336W. In each panel, the underlying f_{esc} distribution is shown with a filled histogram, the f_{esc} distribution of detections with an open histogram, and the mean value for detections is shown with a vertical dotted line and indicated in the top left of each panel. Note that each histogram has been normalized by the maximum value for ease of comparison.

model, we again create 100 mock spectra for each of the 10 000 IGM transmission functions produced at each redshift ($2.9 < z < 3.9$, $\Delta z = 0.1$) with 1500 Å fluxes sampled from an LBG-like distribution. We then repeat our measurements of LyC flux as in previous sections and adopt the flux limits of our fiducial model: F_{lim}(spectroscopy) = 0.025 μJy (∼27.9 mag) and m_{lim}(F336W) = 30.24. The CFHT *u* comparison is not considered here as the relatively shallow nature of these observations results in prohibitively few detections at low $(L_{900}/L_{1500})_{int}$. For a similar reason, we also do not consider LAE-like samples in this section.

We show the resulting $(L_{900}/L_{1500})_{int}$ versus T_{bias} for spectroscopic, LBG-like LyC detections in the left-hand panel of Fig. 13. Similar to the results for our test on detection limits, we find only slight variation in T_{bias} with redshift with a total spread in values of ∼0.03 for all redshifts at a fixed $(L_{900}/L_{1500})_{int}$ above $(L_{900}/L_{1500})_{int} = 0.15$ (again, a fractional definition of T_{bias} will result in significant redshift variation). For reference, we show the location of the fiducial model presented in Section 3.1.1 with the dotted green line and the shaded regions. Slight differences can be attributed to stochasticity as the analysis here represents and independent sample of 1500 Å fluxes and f_{esc} values at the same $(L_{900}/L_{1500})_{int}$ value. Regardless, the results of Fig. 13 are consistent with those of 3.1.1 within errors.

Results for F336W detections are shown similarly in the right-hand panel of Fig. 13. We show results at redshifts where F336W partially probes non-ionizing photons with the dashed lines (i.e. $z < 3.2$). Qualitatively the curves are similar to those in the left-hand panel, with the difference in T_{bias} again attributed to the increased depth of the F336W observational comparison.

Finally, we note that none of the models presented to this point have considered the effects of dust attenuation on the observed LyC flux from mock galaxies. The effect that dust will have on LyC will be to further reduce the observed value of $F(LyC)/F(UV)$ relative to $(L_{900}/L_{1500})_{int}$. In this way, dust attenuation is a third level of degeneracy between f_{esc} and T_{IGM}. Given the low attenuation for LyC detections (e.g. S18), we ignore the effects of dust simply noting that detections should be biased towards galaxies with low dust attenuation (or even none in the case of LAEs, e.g. Fletcher et al. 2019; Nakajima et al. 2020).

4 DISCUSSION

4.1 Correlation between $T_{IGM}(LyC)$ and $T_{IGM}(Ly\,\alpha)$

One major difficulty in accurately measuring f_{esc} from high-redshift galaxies is the unknown value of T_{IGM}. So far, there is no clear observational indicator of T_{IGM}(LyC), which has necessitated statistical methods such as those explored in this paper. In the work of Inoue & Iwata (2008), however, it was argued that the T_{IGM} at Ly α wavelengths may correlate with T_{IGM}(LyC) (their section 4.4, fig. 10). This claim is in direct contrast with previous results of Shapley et al. (2006) who found no such correlation at $z = 3.06$. Inoue & Iwata (2008) suggest that the lack of correlation seen in Shapley et al. (2006) was due to those authors exploring T_{IGM} at only one redshift. Here, we test for a correlation between T_{IGM}(LyC) and T_{IGM}(Ly α) for our simulated IGM transmission functions, noting that our simulations differ from those of Shapley et al. (2006) and Inoue & Iwata (2008) in that we include a CGM component to our H I column density distributions following the work of S18 and Rudie et al. (2013).

To perform this test, we assess all one million IGM sightlines we have produced in Section 2.1, measuring T_{IGM} for LyC at $880 < \lambda_{rest} < 910$ Å and for Ly α at $1050 < \lambda_{rest} < 1170$ Å following Shapley et al. (2006) and Inoue & Iwata (2008). We note, however, that the LyC and Ly α wavelength ranges used in these works are not probing the same redshift range. Thus, we also measure an alternative Ly α wavelength range $1173 < \lambda_{rest} < 1213$ Å, matched to the redshift of LyC in the specified range. In each redshift bin, we measure the spearman rank-order correlation coefficient between T_{IGM}(LyC) and T_{IGM}(Ly α) in both wavelength ranges and also the correlation coefficient of the combined data from all redshift bins.

Fig. 14 shows T_{IGM}(LyC) versus T_{IGM}(Ly α) for all one million sightlines colored by their redshift. Overall, there appears to be a correlation between the two values (albeit with large scatter), however, at any individual redshift such a correlation is less apparent. For T_{IGM}(Ly α) at 1050–1170 Å, we measure correlation coefficients at individual redshifts finding values in the range 0.05–0.08 indicating no correlation with T_{IGM}(LyC) at fixed redshift consistent with Shapley et al. (2006). Considering all redshift bins together, we find a drastic increase in the correlation coefficient to 0.34. This is still lower than the correlation of 0.86 quoted by Inoue & Iwata (2008), however, in this work the authors tested a much wider redshift range from 0.2 to 6.0. Our results combined with those of Inoue & Iwata (2008) suggest that any apparent correlation between T_{IGM} at LyC and Ly α wavelengths is driven only by the fact that both values correlate similarly with redshift (e.g. Fig. 1). For any individual galaxy (or sample) at a given redshift, however, T_{IGM}(Ly α) provides no useful prediction for T_{IGM}(LyC). Indeed, this is apparent from the contours shown in Inoue & Iwata (2008), fig. 10.

As we have pointed out, however, the Ly α wavelength range considered in Shapley et al. (2006) and Inoue & Iwata (2008) is not well matched to the LyC wavelength range they considered. If we instead use our alternative Ly α range, 1173–1213 Å, we find a significant increase in the correlation coefficient at fixed redshift range to 0.32–0.37. Combining the values for all bins we find a

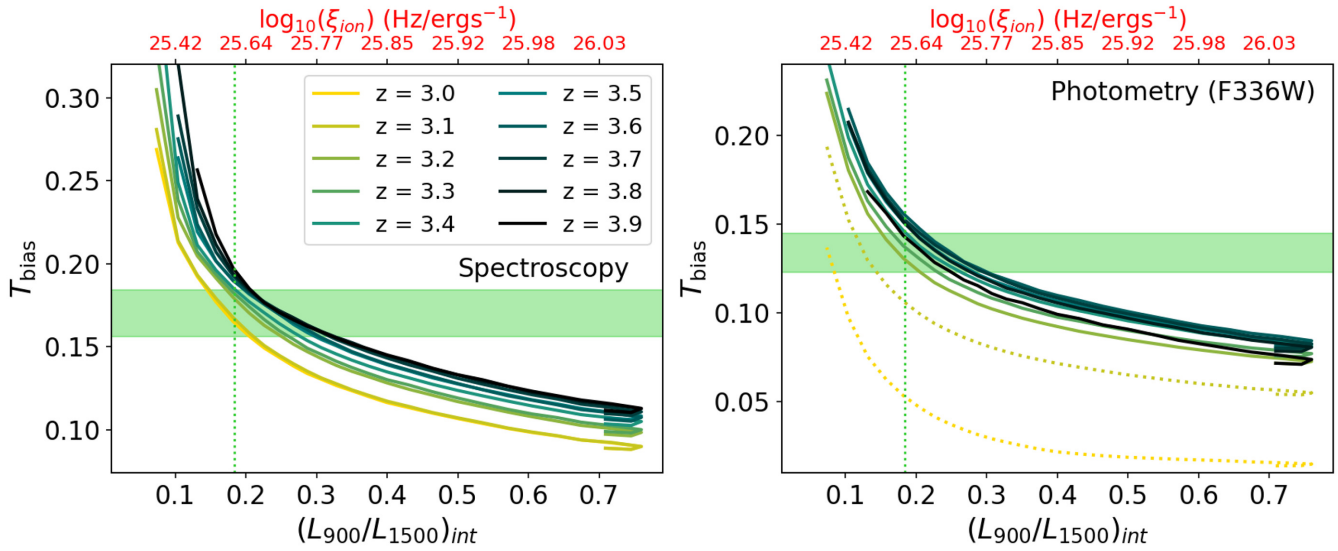

Figure 13. $T_{\rm bias}$ as a function of intrinsic ratio of LyC (at 900Å) to UV (at 1500Å) luminosities for spectroscopy (left) and photometry (right). The solid lines show results in each redshift bin as indicated in each legend, while the dotted lines in the right-hand panel indicate redshifts at which the F336W filter contains contamination from Ly α forest photons as it has not passed fully into the LyC portion of the spectrum. The location corresponding to intrinsic ratios presented in Sections 3.1 and 3.2 is indicated with the dotted green lines and the shaded regions. The top axis of both panels indicates $\xi_{\rm ion}$ for the BPASSv2.1 model at a given $(L_{900}/L_{1500})_{\rm int}$.

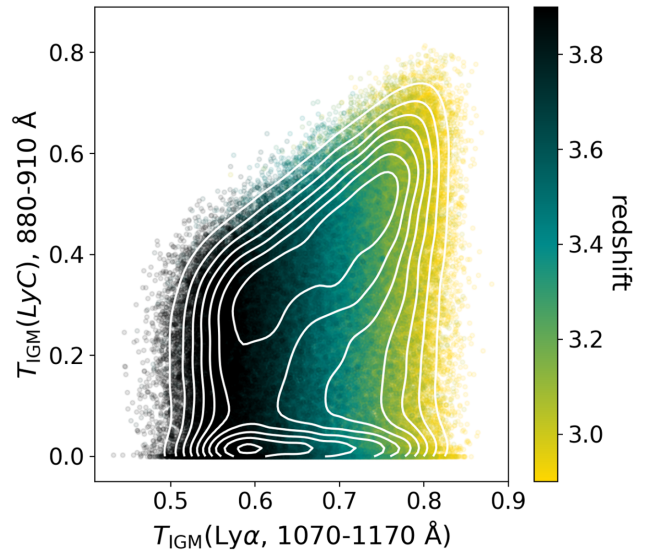

Figure 14. A comparison of $T_{\rm IGM}$ for LyC (880–910 Å) and Ly α (1070–1170 Å) for all one million simulated sightlines. Points are coloured based on their source redshift. We find that the apparent correlation seen between the IGM transmission of LyC and Ly α radiation is driven by the fact that both values exhibit individual redshift dependencies rather than any correlation between these two values. Indeed, there is no apparent correlation between $T_{\rm IGM}$(LyC) and $T_{\rm IGM}$(Ly α) at fixed redshift.

modest increase to 0.45. Thus, we find a weak correlation between $T_{\rm IGM}$ for LyC and Ly α at fixed redshift where the wavelength ranges for these two are well matched. We note that a direct comparison to the results of Inoue & Iwata (2008) and Shapley et al. (2006) may be slightly tenuous as the IGM transmission curves produced there do not include a CGM component while our models do. Indeed, this may be the reason that we find such a large increase in the correlation coefficient at fixed redshift when the wavelength ranges of LyC and Ly α are properly matched. Given the large scatter and the fact that $T_{\rm IGM}$(LyC) is found to be 0 for a range of $T_{\rm IGM}$(Ly α) at fixed redshift, however, we would be hesitant to try and estimate one from the other regardless of the apparent weak correlation.

4.2 Effects of $T_{\rm bias}$ on $f_{\rm esc}$ estimates for samples

The analysis presented in Section 3.1 was designed to predict the average bias for a sample of LyC-detected galaxies, which in turn can be used to estimate the average $f_{\rm esc}$ of the sample (e.g. S18, F19). Thus, it may not be appropriate to blindly apply values measured here to individual galaxies. Here, we test the discrepancy between the average value of $f_{\rm esc}$ for a sample of LyC detections estimated with and without including $T_{\rm bias}$ when compared to the true average $f_{\rm esc}$. This should be seen as a highly simplified test as all mock galaxies represent dust-free BPASSv2.1 models with a fixed $(L_{900}/L_{1500})_{\rm int}$ of 0.18 ($\log_{10}(\xi_{\rm ion}/[{\rm Hz\,erg^{-1}}]) = 26.51$). Real galaxy samples are likely to exhibit a range of $(L_{900}/L_{1500})_{\rm int}$, and will thus decrease the accuracy of $f_{\rm esc}$ estimates when compared to this test.

The typical method of estimating $f_{\rm esc}$ is to employ an equation of the form (or similar to)

$$f_{\rm esc} = \frac{(F_{900}/F_{1500})_{obs}}{(L_{900}/L_{1500})_{int}} \times \frac{1}{\langle T_{\rm IGM}\rangle} \tag{9}$$

noting that the effects of dust attenuation are ignored here. In order to estimate $f_{\rm esc}$ for a given level of $T_{\rm bias}$, equation (9) must be modified in the following way:

$$f_{\rm esc}^{\rm corr} = \frac{(F_{900}/F_{1500})_{\rm obs}}{(L_{900}/L_{1500})_{\rm int}} \times \frac{1}{\langle T_{\rm IGM}\rangle + T_{\rm bias}}. \tag{10}$$

Our test of the recovery of $\langle f_{\rm esc}\rangle$ for a sample of spectroscopically LyC-detected galaxies is performed on the mock observations described in Section 2.3. We first select those mock galaxies with output $880 < \lambda_{\rm rest} < 910$ Å fluxes above the detection limit of 0.025 μJy. We then perform 5000 trials in which we randomly select 15 mock LyC detections (matched to the number of detections in S18) and measure

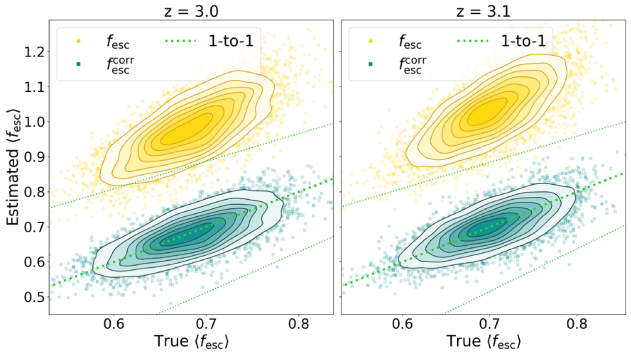

Figure 15. Comparison of $\langle f_{esc} \rangle$ computed via equation (9; gold) and equation (10; cyan) compared to the true $\langle f_{esc} \rangle$ at $z = 3.0$ (left) and $z = 3.1$ (right). Here, we perform 5000 trials in which 15 LyC-detected galaxies are selected at random (comparable to the number detected in S18) from among the one million mock galaxies produced at each redshift as decribed in Section 2.3. We calculate the average $(F_{900}/F_{1500})_{obs}$ among the 15 galaxies and use this value to estimate $\langle f_{esc} \rangle$ using equations (9) and (10). The one-to-one relation is shown with the thick dotted line, while the thin dotted lines represent the average 68 percentile spread of the 15 galaxies selected in individual trials (more description in text), which we find to decrease roughly linearly with increasing the mean f_{esc} for a given trial.

$\langle (F_{900}/F_{1500})_{obs} \rangle$ of this subsample. For each trial, we calculate the average f_{esc} using equations (9) and (10) and compare this with the true $\langle f_{esc} \rangle$ for the 15 selected detections.

The results of this test at $z = 3.0$ and $z = 3.1$ for our $\eta = 0.5$ f_{esc} PDF model are shown in Fig. 15, though we find similar results for the flat f_{esc} PDF of our fiducial model. Here, we plot the true $\langle f_{esc} \rangle$ versus two estimated values. The gold and cyan contours show the distribution for $\langle f_{esc} \rangle$ estimated using equations (9) and (10), respectively. The thick dotted green line shows the one-to-one relation. The thin green lines are meant to be representative of the average 68 percentile spread of the 15 galaxies from any individual trial. To produce these lines, we measure the 68 percentile lower and upper bounds and the average values of f_{esc} for the 15 galaxies from each of the 5000 trials. We find that the upper and lower bounds for a given trial decrease roughly linearly with increasing mean f_{esc} (albiet with significant scatter), thus we fit each bound with a straight line as a function of mean f_{esc}. In this way, we are attempting to illustrate, roughly, the expected speard in f_{esc} values for a random selection of 15 LyC-detected galaxies having a given mean f_{esc} value.

At both redshifts, there is good agreement between f_{esc}^{corr} and the true value, while failing to account for T_{bias} results in an overestimate of the average f_{esc}. The level of overestimation is lower at $z = 3.0$ due to the fact that f_{esc} in equations (9) and (10) depends on the reciprocal of T_{IGM}, which is decreasing with redshift towards 0. At $z = 3.1$, Only $\sim$1.4 per cent of the estimated $\langle f_{esc} \rangle$ values calculated using equation (9) fall within the range of typical 'true' f_{esc} values for our detected sample (noting this percentage is stochastic). At higher redshifts this falls to 0 per cent. Considering f_{esc}^{corr}, we find that, typically, less than 1 per cent of trials fall outside of the rough confidence intervals presented in Fig. 15. This test illustrates that not accounting for T_{bias} when estimating the stacked f_{esc} for detected galaxies can result in a significant overestimate of the true value.

Of course, as has been repeated throughout this work, the absolute differences between f_{esc} and f_{esc}^{corr} (as well as the fractional decrease) will have some dependence on the details of our method for producing IGM transmission curves (e.g. $N_{H\,I}$ distributions), the assumed value(s) of $(L_{900}/L_{1500})_{int}$, the assumed f_{esc} PDF, the input distribution of 1500 Å fluxes, etc. In addition, the inclusion of dust, choice of dust curve, and any assumed dependence between $E(B-V)$ and f_{esc} will further affect these results. Although not shown, we also performed the test presented here with dust attenuation included following the method outlined in Section 4.4 [where $E(B-V)$ values are sampled from a distribution characterized by the observed values from S18] and find similar results with a similar level of scatter. This of course assumes that both the average $E(B-V)$ for detected galaxies as well as the exact form of the attenuation curve is precisely known. Inevitably, these values will be highly uncertain for real observations resulting in a higher level of scatter. Providing more realistic tests of the associated effects on our stacking, while possible, would be highly model dependent, thus not particularly useful.

The fact that T_{IGM} for LyC-detected galaxies is expected to be larger than $\langle T_{IGM} \rangle$ at a given redshift will be true regardless of the exact implementations, however. Thus, the purpose of the illustration presented here is simply to highlight the fact that the assumption that $\langle T_{IGM} \rangle$ is representative of IGM sightlines towards LyC-detected galaxies will result in an overestimation of f_{esc}. Given that T_{bias} increases with decreasing observational depth, the overestimation of f_{esc} will be the higher for shallower LyC surveys.

4.3 Survey detection rate versus f_{esc} PDF

As we have shown in Section 3.2, the value of $\langle f_{esc} \rangle$ inferred for stacked samples of LyC detections will depend on the PDF assumed for f_{esc}. It has been repeated throughout this work that, observationally, there appears to be a preference for low (or zero) f_{esc} from high-redshift galaxies (e.g. Japelj et al. 2017; Smith et al. 2018; Bian & Fan 2020). This creates a chain of circular reasoning, however, as accurate measurements of f_{esc} thus requires knowledge of the PDF of f_{esc}, which seemingly requires accurate measurements of f_{esc} to determine. The way forward is to determine an observational metric that can help to determine the PDF f_{esc} that is independent of the individual values of f_{esc}.

In this section, we propose that the detection rates of LyC from dedicated surveys can be used to probe the parameters of a given f_{esc} PDF. We construct two mock versions of the surveys of S18, F19, and M20, one with a flat f_{esc} PDF and one with an exponentially declining f_{esc} PDF. In the latter case, we tune the value of η (see equation 8) to match the observed detection rate of a given survey (more description to follow). In each case, we again use the same fixed input BPASSv2.1 SED model as our fiducial model with $(L_{900}/L_{1500})_{int} = 0.18$. In all cases, the input 1500 Å fluxes are sampled from a distribution matched to the fluxes reported by each of those surveys. Thus, in this case, the F19 sample, which is made up of LAEs, have a characteristic 1500 Å flux that is lower than that of the LBG samle of S18 at the same redshift resulting in a lower relative LyC flux (see Fig. 4). This is important as the selection method of a given sample strongly influences the distribution of galaxy properties included (e.g. typical 1500 Å flux, $(L_{900}/L_{1500})_{int}$, among others), which ultimately determine the output LyC fluxes, and thus the detectability of a given galaxy. Therefore, the toy model presented here is primarily for illustrative purposes.

The set of inputs described above is combined with our T_{IGM} sightlines to produce an output sample of LyC fluxes. In the case of S18 and F19, we simply use the T_{IGM} functions already produced, noting that this requires all of our mock galaxies to be at discrete redshifts with $\Delta z = 0.1$. For S18, we match the observed redshift distribution in each bin from that work and for F19 all galaxies are

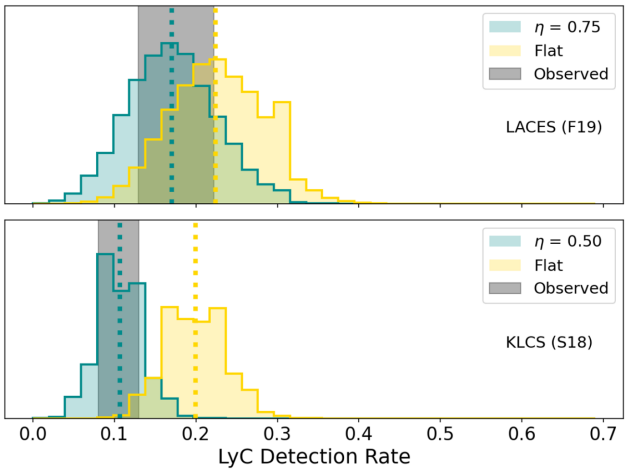

Figure 16. Detection rate distributions for our mock LACES (top) and KLCS (bottom) surveys. In each case, we create 50 000 mock spectra at the respective survey redshifts following Section 2.3, however, we now include the effects of dust attenuation for the S18 comparison (see text). The observed detection rates are shown in grey, while the detection rates assuming a flat and exponentially declining f_{esc} PDF are shown in gold and cyan, respectively. In each case, the value of η for the exponentially declining PDF is coarsely tuned to match the detection rate of a given survey.

simulated at $z = 3.1$. As M20 explores significantly higher redshifts, we simply randomly sample values across the full redshift range (matched to the observed distribution from that work) and create new T_{IGM} functions each time. For each survey we produce 10 000 mock observations. We then randomly draw subsamples from these mock observations with sizes matched to the observed sample sizes in each paper and measure the detection rates of LyC for each subsample with detection rates of 0.025 μJy (∼27.9 mag), 30.24, and 27.82 mag for S18, F19, and M20, respectively. We perform this test with a few different η values for the exponential f_{esc} PDF, and coarsely tune the model such that the average detection rate falls within the range quoted for each survey.

The results of our test for KLCS and LACES are shown in Fig. 16. In each panel, the detection rate distribution for the tuned, exponentially declining model is shown in cyan (with the tuned η value in the legend) and the distribution for the flat model is shown in gold. For LACES, the observed detection rate range is defined by either only considering their 'gold' sample (low) or considering the 'gold' plus 'silver' samples (high) and for KLCS we take their detection rate of 15/124 ∼ 0.12. In the case of KLCS, the flat f_{esc} PDF model is seen to predict a detection rate that is too large to reproduce the survey in question. While the $\eta = 0.5$ model is well matched to the observed detection rate. In the case of LACES, however, though the average detection rate for the flat model is close to the upper limit for the detection rate of that suvey, it is difficult to rule out a flat PDF. The coarsely matched exponential model requires a relatively high value of $\eta = 0.75$. From Fig. 12, we expect that the inferred f_{esc} values from this model will not differ significantly from a flat distribution. In the case of our mock M20 test, we were unable to reproduce the high detection rate reported in the paper, which falls in the range 0.02–0.11 (1–5 of 44) depending on the reliability cut for the LyC-emitting galaxy candidates from that work. For our mocks, we find an overall detection rate from the flat f_{esc} PDF (which will give the highest detection rate) of 0.005, thus only a small fraction of random selections of 44 galaxies will even contain one detection.

Taken together, this toy model test for our three comparison samples provides strong evidence that the underlying f_{esc} PDFs will be sensitive to the selection bias of the galaxy sample in question. In the case of KLCS and LACES, the former probes the bright end of the UV luminosity function characterized by LBGs while the latter significantly fainter LAEs. The fact that the detection rate of KLCS requires the f_{esc} PDF to be skewed towards 0, while LACES is not inconsistent with a flat f_{esc} PDF points towards a scenario in which faint galaxies, on average, have a f_{esc} PDF less biased towards 0 (similar to the results of Finkelstein et al. 2019). Our inability to reproduce the high detection rate of M20, even employing a flat f_{esc} PDF, suggests that this sample may be biased towards high values of f_{esc} (though we have not tested such a model here). Interestingly, the goal of M20 was to provide a methodology for preferentially selecting high f_{esc} galaxies, consistent with the toy model presented here. The key point highlighted here is that we have shown the calculation of f_{esc} to be sensitive to the underlying PDF (e.g. Fig. 12), which is in turn appears to depend on sample selection. Thus, a consideration of the f_{esc} PDF should be considered in particular when comparing inferred f_{esc} values between disparate samples (e.g. LAEs versus LBGs).

We reiterate that the exponentially declining f_{esc} PDF favoured here is simply an ad hoc solution chosen for its bias towards low f_{esc} values and a preference for $f_{esc} = 0$. This selection was motivated by the low detection rate of such emission and the, generally, low estimates of the average f_{esc} for large galaxy samples (e.g. Vanzella et al. 2010; Grazian et al. 2016; Smith et al. 2018). The true functional form of the PDF of f_{esc} is very likely more complex and may include dependencies on galaxy properties such as, e.g. stellar mass (Finkelstein et al. 2019; Naidu et al. 2020). Further clarification of this issue will require larger samples of LyC detections at $z > 3$ that would be greatly aided by more sensitive instrumentation at u-band wavelengths. It is also likely that inputs from high-resolution, hydrodynamics simulations of high-redshift galaxies that include full radiative transfer can help greatly with the interpretation of detections (and non-detections), though running such simulations is computationally expensive. Regardless, we show here evidence that the most likely PDF for f_{esc} for LBG like galaxies favours a model with a reasonable bias towards low f_{esc}.

4.4 Dust attenuation

To this point, we have avoided one key topic in the study of optical and UV radiation from star-forming galaxies: dust attenuation. In general, the level of attenuation at fixed $E(B - V)$ increases with decreasing λ_{rest} such that UV wavelengths experience the highest levels of attenuation (i.e. lowest transmission) irrespective of the functional form of the assumed attenuation curve (e.g. Gordon & Clayton 1998; Calzetti et al. 2000; Reddy et al. 2016, etc). This statement, of course, assumes that extending the chosen attenuation curve to short wavelengths ($\lesssim$1500 Å) is reasonable. We acknowledge that Buat et al. (2002) have investigated dust attenuation at 900 Å in a handful of local star-forming galaxies and Weingartner & Draine (2001) have explored theoretical models of dust attenuation in a similar regime (based on the Magellanic clouds), however, there applicability to high-redshift galaxies is also uncertain. Regardless, the expected high level of attenuation at LyC wavelengths may lead one to expect that galaxies with a high enough LyC flux to be detected in current surveys should be biased towards low attenuation. Indeed, LyC detections from KLCS all have $\langle E(B - V)\rangle = 0.045$ (and 0.129 for full LBG parent sample, S18), and those of LACES all exhibit negligible attenuation ($E(B$

$-V) < 0.07$, $\langle E(B-V)\rangle \simeq 0.01-0.03$, F19, Nakajima et al. 2020).

Regardless, to expect all LyC-emitting galaxies to contain negligible amounts of dust is likely too simplistic. Thus, some consideration of the effects of dust in the interpretive framework for f_{esc} calculations outlined in this paper is warranted. We advocate a methodology similar to that outlined in F19. First, a determination of the stellar $E(B-V)$ value should be computed based on the available photometric data for a given sample of objects. This can be achieved through full SED fitting or through calibrations such as those based on the UV slope, β (e.g. Meurer, Heckman & Calzetti 1999). In the case of SED fitting, we advocate a method only incorporating bands redward of Lyα, as shorter wavelengths are strongly affected by IGM attenuation (e.g. effects not intrinsic to the galaxy) that should be treated independently to avoid added degeneracy in the SED model. The effects of including or omitting flux with wavelengths shortward of Lyα during the SED fitting process will be tested in future work (Bassett et al., in preparation). The computed $E(B-V)$ is combined with a choice of dust attenuation curve, $k(\lambda)$, to correct the observed 1500 Å flux to the 'intrinsic', dust-free, value. Finally, the chosen input SED template for a given sample (either computed through SED fitting or simply selecting a template with a reasonable value of $(L_{900}/L_{1500})_{int}$) is scaled to match the corrected 1500 Å flux. Through this process, the intrinsic LyC flux can be determined, noting this value will be dependent on the selection of the intrinsic SED.

From the intrinsic LyC flux calculated in this manner, one can then determine the expected value of f_{esc} by comparing with the observed value. In this way, any attenuation of LyC flux due to dust is incorporated into the definition of f_{esc}, as pointed out by F19 (i.e. there is no distinction between dust attenuation and absorption of LyC by neutral hydrogen). We also follow the methodology of F19 who allow f_{esc} for a given value of $E(B-V)$ to only be as large as the transmission allowed by the extrapolated dust attenuation curve. This is reasonable as, in the case of a galaxy with relatively large $E(B-V)$, a value of $f_{esc} = 1.0$ would imply zero dust attenuation for LyC and high attenuation at 1500 Å. We note, however, that such a case is not entirely impossible given LyC emission is often dominated by stellar populations with ages < 10 Myr,' while stellar populations as old as a few hundred Myr can provide significant flux at 1500 Å (e.g. Eldridge et al. 2017), thus the emission at each wavelength may originate from different locations within a given galaxy.

We do note, however, that this maximum f_{esc} allowed by the assumed attenuation curve is highly model dependent. For example a Small Magellanic Cloud attenuation curve (e.g. Gordon & Clayton 1998) will have a much higher attenuation at LyC wavelengths when compared to either a Calzetti et al. (2000) or Reddy et al. (2016) attenuation curve with the same 1500 Å attenuation. This results from the fact that the extension of the functional form of either a Calzetti et al. (2000) or Reddy et al. (2016) $k(\lambda)$ is significantly flatter at $\lambda < 1500$ Å than that of Gordon & Clayton (1998). This caveat is important to keep in mind when considering the possible 'maximum' f_{esc} allowable for a given value of $E(B-V)$.

4.5 LyC detections at other redshifts

The study of LyC escape from galaxies in ground-based studies is limited to redshifts $\gtrsim 2.8$ due to the low atmospheric transmission of UV photons. This limitation is not suffered by space-based instrumentation, thus, studies of LyC at lower redshifts can be performed at significantly lower redshifts with satellite instrumentation. In particular, LyC has been detected at $z \sim 2.5$ by Bian et al. (2017) using the *HST*-WFC3 F275W filter, and recently at $z = 1.42$ by Saha et al. (2020) with the Ultraviolet-Imaging Telescope on board AstroSat. We also note that there has been significant activity in spectroscopic detection of LyC from green pea galaxies at $z \sim 0.3-4$ with *HST* COS (e.g. Izotov et al. 2016, 2018). At such low redshifts, however, IGM transmission should be negligible, thus these studies are not of particular relevance to the study of T_{bias}.

Here, we focus on providing predictions for detection of LyC within the Ultraviolet Imaging of the Cosmic Assembly Near-infrared Deep Extragalactic Legacy Survey Fields (UVCANDELS; PI: Teplitz, PID 15647), a ~430 arcmin^2, 164-orbit Cycle 26 UV *HST* program. UVCANDELS will provide 3-orbit depth of WFC3/275W and parallel ACS/F435W in four CANDELS fields: GOODS-N, GOODS-S, EGS, and COSMOS.

For our predictions, we follow a similar procedure outlined in Section 4.3, however, here we have produced 10 000 IGM transmission curves at both $z = 2.4$ and $z = 4.4$ for the purpose of providing mock observations of LyC using the WFC3/F275W and ACS/F435W filters, respectively. To sample the input 1500 Å fluxes or this comparison, we sample from UV luminosity functions of Moutard et al. (2020) derived from the CLAUDS survey for $z = 2.4$ and from fits to B-band dropouts ($z \gtrsim 3.8$) from Bouwens et al. (2015) for $z = 4.4$. In both cases, we use luminosity functions described by a Schechter function with $\alpha = -1.4$, $\phi^* = 2.708 \times 10^{-3}$, and $M^* = -20.623$ at $z = 2.2$ and $\alpha = -1.64$, $\phi^* = 1.97 \times 10^{-3}$, and $M^* = -20.88$ at $z = 4.4$. For all mock galaxies, we assume a value of $(L_{900}/L_{1500})_{int}$ of 0.18.

To sample the $\lambda_{rest} \sim 1500$ Å flux for mock galaxies, we measure our SED with the ACS/F435W and WFC3/F814W for $z = 2.4$ and $z = 4.4$, respectively. The 5σ depths of each filter are matched to the observations at 27.0 mag for F275W, 28.0 for F435W, and 28.4 for F814W. For the best chance of detecting LyC emission, we produce roughly 100 000 mock observations of galaxies at each redshift, significantly more than should be expected in the UVCANDELS volume. We also assume a flat f_{esc} PDF, to further increase the possibility of producing galaxies with very bright LyC flux.

The results of this test are shown in Fig. 17. The top row shows the non-ionizing UV versus LyC magnitudes (observational band is redshift dependent) and the bottom row show the histograms of F275W and F435W magnitudes in logscale. In both panels, we show the magnitude limits of UVCANDELS for respective LyC probing bands with a vertical dashed line. For galaxies with $(L_{900}/L_{1500})_{int} = 0.18$, the 5σ limits of UVCANDELS are too shallow to detect individual galaxies within the UVCANDELS footprint as the brightest. In the event that UV bright galaxies with significantly higher $(L_{900}/L_{1500})_{int}$ exist within the UVCANDELS footprint, it may be possible that one or two individual detections will be found. We conclude that pushing observations to a depth of 30 mag and beyond in small, targeted fields (i.e. similar to the $z = 3.1$ observations of Fletcher et al. 2019) is likely to be more fruitful than shallow searches over large areas such as UVCANDELS.

Given the expected faintness of LyC emission, wide area surveys such as UVCANDELS will likely rely on stacking analysis in order to estimate the average f_{esc} for galaxy subsamples. In this scenario, prior information regarding the likelihood of escaping LyC emission (e.g. evidence of a hard ionizing spectrum or high Lyα escape, if available) will be useful. This is due to the fact that, although high LyC flux is more common for UV bright galaxies, galaxies with the same UV brightness are also commonly found with relatively low LyC flux (as shown in Fig. 17). Similarly, we find galaxies with relatively faint non-ionizing UV flux with relatively high LyC flux. Thus, simply stacking the galaxies with the highest 1500 Å flux does

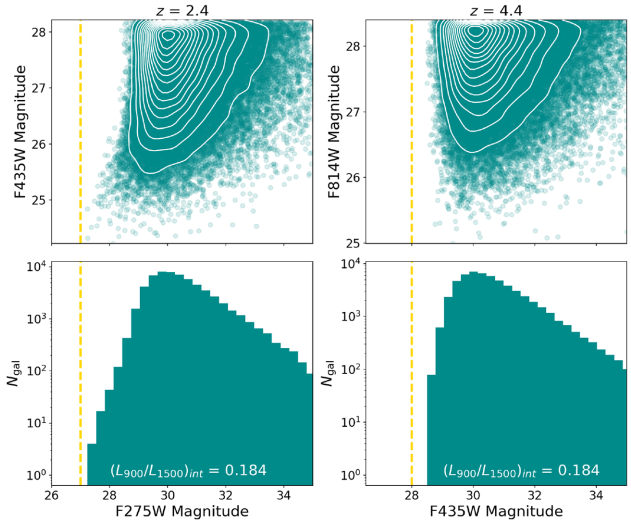

Figure 17. UV magnitudes of mock star-forming galaxies at $z = 2.4$ and $z = 4.4$ as observed by the UVCANDELS survey. Here, 1500 Å fluxes are sampled from the $z \sim 2.5$ UV luminosity function of Moutard et al. (2020) and from the $z \sim 4.0$ UV luminosity function of Bouwens et al. (2015) with depths matched to UVCANDELS. *Top row:* LyC versus non-ionizing UV magnitudes of mock observations. *Bottom row:* histograms of magnitudes for LyC probing bands. In all panels, the vertical dashed line indicates the depths of UVCANDELS observations. Here, mock galaxies are produced as dust-free, exponentially declining SFR BPASSv2.1 SEDs with $(L_{900}/L_{1500})_{\rm int} = 0.184$, and assuming a flat $f_{\rm esc}$ PDF. We note that a larger value of $(L_{900}/L_{1500})_{\rm int}$ can produce a handful of individual LyC-detected galaxies.

not guarantee that the galaxies with the highest LyC flux have been chosen.

Finally, we note a few caveats to this analysis. First, this analysis has been performed using $T_{\rm IGM}$ curves produced independently, while UVCANDELS covers four individual fields. In the event that there is strong correlation in $T_{\rm IGM}$ across the field, the resulting LyC fluxes may be systematically higher (in the case of high $T_{\rm IGM}$) or lower (in the case of low $T_{\rm IGM}$) for one particular field. Consideration of the correlation of $T_{\rm IGM}$ between sources in individual fields of a given area may require dedicated analysis of large scale simulations of the H I distributionns and is beyond the scope of this work. And secondly, this analysis has ignored variation in $(L_{900}/L_{1500})_{\rm int}$ (as noted), assumed no dust attenuation, and employed a flat $f_{\rm esc}$ PDF, all three of which will affect our resulting LyC fluxes.

4.6 Observed versus true $f_{\rm esc}$

Ultimately, the ongoing search for LyC emission from high-redshift galaxies is closely connected with our understanding what types of galaxies are responsible for reionizing the Universe. Characterizing the population of strong LyC emitters will be key to informing our picture of the topological evolution of ionized regions during the EoR (Seiler et al. 2018). There exists, however, an inherent difficulty regarding the interpretation of $f_{\rm esc}$ values measured observationally due to the complex geometry of LyC escape from galaxies, independent of $T_{\rm IGM}$. Indeed various models have been hypothesised that may provide slightly different interpretations of the detected LyC flux in the context of measuring $f_{\rm esc}$. A detailed discussion of various LyC escape models can be found in section 9.4 of S18.

Crucially, it has been pointed out (e.g. Bassett et al. 2019; Barrow et al. 2020) that the detection of LyC from any individual galaxy is reflective of only the fraction of LyC that is able to escape into our single line of sight. There is still no reliable way of inferring if the observed $f_{\rm esc}$ value is reflective of $f_{\rm esc}$ in all directions, i.e. the 3D $f_{\rm esc}$ (though intriguing indirect measurement techniques for the 3D $f_{\rm esc}$ have been proposed, which warrant further exploration within an anisotropic LyC escape scenario, e.g. Zackrisson, Inoue & Jensen 2013; Yamanaka et al. 2020). Similarly, the lack of LyC emission from any individual galaxy is not evidence of $f_{\rm esc} = 0.0$ as large quantities of LyC photons could be escaping in directions other than our line of sight. As we have shown, the value of $f_{\rm esc}$ is dependent on the assumed underlying PDF and current detection rates may disfavour a flat distribution. One way to provide a theoretically sound basis for our assumptions on the PDF of $f_{\rm esc}$ for galaxies or galaxy samples is through the careful consideration of high-resolution hydrodynamical simulations.

LyC escape can be measured in such simulations by applying full radiative transfer, then measuring $f_{\rm esc}$ from a large number of sightlines towards the galaxy. This method provides the full three-dimensional $f_{\rm esc}$ at a given time and has shown that even for individual galaxies $f_{\rm esc}$ is highly variable and can swing from 0 to 1 within 100 Myr (Paardekooper et al. 2015; Trebitsch et al. 2017; Rosdahl et al. 2018), though there may be some mass dependence on the 3D $f_{\rm esc}$ PDF. It has been shown, however, that for a galaxy with given 3D $f_{\rm esc}$ value the value of $f_{\rm esc}$ in any particular sightline may vary from 0 to values larger than the true 3D value (e.g. Paardekooper et al. 2015, fig. 13). Thus, to construct the underlying $f_{\rm esc}$ PDF for a given sample of galaxies may require the combination of the 3D $f_{\rm esc}$ of galaxies (with possible dependencies on mass or other properties) with the probability distribution of 2D $f_{\rm esc}$ (line of sight) for a given 3D $f_{\rm esc}$ value. Disentangling the various dependencies on these underlying PDFs will require suites of high-resolution simulations with full radiative transfer, but is of the utmost importance in interpreting the 2D $f_{\rm esc}$ values from observations with the true 3D $f_{\rm esc}$ distributions. Ultimately it is the full 3D $f_{\rm esc}$ values from galaxies that are of interest in the context of the EoR, which can only be connected to our 2D observational results through such a complex line of reasoning as is described here.

5 SUMMARY AND CONCLUSIONS

In this paper, we have explored the level of bias in the IGM transmission, $T_{\rm IGM}$, for galaxies with LyC detections at $z = 3-4$ under the observational limits imposed by current instruments and surveys. Our tests were performed by simulating one million IGM transmission functions in our redshift range of interest and applying these to empirically motivated mock galaxy spectra constructed from the BPASSv2.1 models (Eldridge et al. 2017). We have also tested how the level of IGM transmission bias, $T_{\rm bias}$, depends on both the assumed PDF of $f_{\rm esc}$ and SED shape (which controls $(L_{900}/L_{1500})_{\rm int}$, a key value for measuring $f_{\rm esc}$). Our analysis has included modeling designed to approximate both spectroscopic and photometric LyC detections from recent surveys of Steidel et al. (2018), Fletcher et al. (2019), and Meštrić et al. (2020).

Broadly, we find that, in all cases the average value of $T_{\rm IGM}$ at LyC wavelengths for galaxies with LyC detections is found to be larger than the average $T_{\rm IGM}$ for all simulated sightlines at the same redshift. This results from the fact that the underlying $T_{\rm IGM}$ distribution at 880 Å $< \lambda_{\rm rest} <$ 910 Å is bimodal with the stronger peak at $T_{\rm IGM} = 0$, but the simple fact that the galaxy has been detected means that $T_{\rm IGM} \neq 0$. Thus, the $T_{\rm IGM}$ distribution for LyC-*detected* galaxies is unimodal with a peak at relatively high $T_{\rm IGM}$, while the mean for all sightlines falls below this due to the inclusion of the $T_{\rm IGM} = 0$ peak. The result is that the assumption of a mean $T_{\rm IGM}$ for all sightlines

when calculating $\langle f_{esc} \rangle$ for a sample of LyC-detected galaxies results in an overestimate of the true value. This result is similar to the recent results of Byrohl & Gronke (2020) for Lyα transmission. Thus, it is becoming clear that, while tempting, using a single statistic (e.g. median or mean) when considering T_{IGM} for individual objects provides misleading results for LyC detected samples. Considering samples that include (are composed entirely of) LyC non-detected galaxies, the use of $\langle T_{IGM} \rangle$ when calculating upper limits on $\langle f_{esc} \rangle$ is appropriate, however. The remainder of our conclusions can be summarized as follows:

(i) Assuming the an LBG-like UV flux distribution and applying detection limits of Steidel et al. (2018), Fletcher et al. (2019), and Meštrić et al. (2020) we estimate minimum levels of T_{bias} to be $\sim$0.15, $\sim$0.11, and $\sim$0.22 for each survey, respectively.

(ii) In the case of a UV flux distribution more characteristic of LAE sample (e.g. those of Fletcher et al. 2019), a higher T_{bias} should be expected. In this case, mock *HST* F336W observations similar to Fletcher et al. (2019), the minimum T_{bias} increases to $\sim$0.21.

(iii) We have shown in Section 3.2 that, although T_{bias} does not increase significantly assuming an f_{esc} PDF mildly biased towards 0, there may be a slight decrease in the recovered f_{esc} value in such a model.

(iv) We have also demonstrated that the current detection rates of LyC radiation from surveys may reflect information regarding the underlying f_{esc} PDF. Our simplified model presented in Section 4.3, for example, appears to slightly disfavour a flat f_{esc} PDF for LBGs (e.g. Steidel et al. 2018), though this may not be the case for LAE samples (e.g. Fletcher et al. 2019).

This final point may suggest that fainter galaxies, represented by LAE samples, are more likely to exhibit a higher f_{esc} than bright galaxies, represented by LBGs. Such a scenario is in agreement with other recent studies (e.g. Finkelstein et al. 2019). Our comparisons in this context in Section 4.3 with the detection rates of Steidel et al. (2018) and Fletcher et al. (2019) are still in the realm of low statistical significance. Thus, confirmation of these results will require larger samples of LyC-detected galaxies on which to perform a similar analysis.

Of course, all of our results will depend on the various input parameters of our models including the assumed distribution of 1500 Å (rest frame) fluxes, our treatment (or lack thereof) of dust attenuation, our assumptions regarding the intrinsic luminosity ratio $[(L_{900}/L_{1500})_{int}]$ of galaxies, and even the details of our methods for producing T_{IGM} functions (e.g. H I distribution functions). Thus, we do not claim that the absolute values of T_{bias} from this work to be in any way definitive. The purpose of this work is to highlight the ways in which different assumptions regarding the underlying distributions of T_{IGM} and f_{esc} affect our attempts to estimate f_{esc} from galaxies. It is clear that significant theoretical work is still required to better understand these PDFs that are critical to our interpretation of LyC detections from observations.

From an observational point of view, it is also clear that larger samples of LyC detections will be essential in disentangling the various dependencies on f_{esc} (e.g. stellar mass, SFR, etc.). It is possible that more efficient searches can be conducted in the near future with a focus on increasing both depth and field of view (FOV). Indeed, we find the highest detection rates among our mock surveys for our mock LACES survey (Fletcher et al. 2019, Section 4.3), primarily due to those observations reaching 30.24 mag. The drawback is that this study is performed with WFC3, an instrument with a relatively small FOV. One possible future instrument that may push LyC surveys to the next level is the Keck Wide Field Imager (Gillingham et al. 2020) that is expected to achieve a signal to noise of $\sim$2 at 30th magnitude in the *u* band across a 1° diameter FOV in just under 8 h of exposures (private communication). From our mock LACES survey, we estimate that $\sim$50 per cent of all simulated galaxies fall in the magnitude range between 30 and 32. Thus, the era of large samples of known LyC-emitting galaxies may be near.

ACKNOWLEDGEMENTS

This research was conducted by the Australian Research Council Centre of Excellence for All Sky Astrophysics in 3 Dimensions (ASTRO 3D), through project number CE170100013. The authors wish to thank Chris Blake, Adam Batten, and Katinka Geréb for useful and illuminating discussions. We also wish to thank our referee, Akio K. Inoue, for careful consideration of the manuscript, which has resulted in an improved focus within the context of current studies exploring LyC emission from galaxies at high redshift. Results presented in this work have made extensive use of the PYTHON3 programming language (Van Rossum & Drake 2009) and, in particular, the authors wish to acknowledge the the NUMPY (Harris et al. 2020), MATPLOTLIB (Hunter 2007), and SCIPY (Virtanen et al. 2020) packages. MR and LP acknowledge support from *HST* programs 15100 and 15647. Support for Program numbers 15100 and 15647 were provided by NASA through a grant from the Space Telescope Science Institute, which is operated by the Association of Universities for Research in Astronomy, Incorporated, under NASA contract NAS5-26555.

DATA AVAILABILITY

Simulated data used in this work are produced primarily using publicly available codes found at https://github.com/robbassett as well as publicly available galaxy SED models from the BPASS collaboration (Eldridge et al. 2017). Observational data used for comparison is available from publications associated with those surveys.

REFERENCES

Barrow K. S. S., Robertson B. E., Ellis R. S., Nakajima K., Saxena A., Stark D. P., Tang M., 2020, ApJ, 902, L39
Bassett R. et al., 2019, MNRAS, 483, 5223
Becker G. D., Hewett P. C., Worseck G., Prochaska J. X., 2013, MNRAS, 430, 2067
Bershady M. A., Charlton J. C., Geoffroy J. M., 1999, ApJ, 518, 103
Bian F., Fan X., 2020, MNRAS, 493, L65
Bian F., Fan X., McGreer I., Cai Z., Jiang L., 2017, ApJ, 837, L12
Boutsia K. et al., 2011, ApJ, 736, 41
Bouwens R. J., Illingworth G. D., Oesch P. A., Caruana J., Holwerda B., Smit R., Wilkins S., 2015, ApJ, 811, 140
Bouwens R. J., Smit R., Labbé I., Franx M., Caruana J., Oesch P., Stefanon M., Rasappu N., 2016, ApJ, 831, 176
Buat V., Burgarella D., Deharveng J. M., Kunth D., 2002, A&A, 393, 33
Byrohl C., Gronke M., 2020, A&A, 642, L16
Calzetti D., Armus L., Bohlin R. C., Kinney A. L., Koornneef J., Storchi-Bergmann T., 2000, ApJ, 533, 682
Carswell R. F., Webb J. K., 2014, Astrophysics Source Code Library, record ascl:1408.015
Eldridge J. J., Stanway E. R., Xiao L., McClelland L. A. S., Taylor G., Ng M., Greis S. M. L., Bray J. C., 2017, Publ. Astron. Soc. Aust., 34, e058
Fan X., Carilli C. L., Keating B., 2006, ARA&A, 44, 415
Fernández-Soto A., Lanzetta K. M., Chen H. W., 2003, MNRAS, 342, 1215

Finkelstein S. L. et al., 2019, ApJ, 879, 36
Fletcher T. J., Tang M., Robertson B. E., Nakajima K., Ellis R. S., Stark D. P., Inoue A., 2019, ApJ, 878, 87 (F19)
Forrest B. et al., 2017, ApJ, 838, L12
Giallongo E., Cristiani S., D'Odorico S., Fontana A., 2002, ApJ, 568, L9
Gillingham P., Cooke J., Glazebrook K., Mould J., Smith R., Steidel C., 2020, in Ellis S. C., d'Orgeville C., eds, Advances in Optical Astronomical Instrumentation 2019, Proc. SPIE Conf. Ser., Vol. 11203, SPIE, Bellingham, p. 112030F
Gordon K. D., Clayton G. C., 1998, ApJ, 500, 816
Grazian A. et al., 2016, A&A, 585, A48
Greig B., Mesinger A., 2017, MNRAS, 472, 2651
Harris C. R. et al., 2020, Nature, 585, 357
Hasinger G. et al., 2018, ApJ, 858, 77
Hopkins P. F., Richards G. T., Hernquist L., 2007, ApJ, 654, 731
Hui L., Rutledge R. E., 1999, ApJ, 517, 541
Hunter J. D., 2007, Comput. Sci. Eng., 9, 90
Inoue A. K., Iwata I., 2008, MNRAS, 387, 1681
Inoue A. K., Iwata I., Deharveng J.-M., Buat V., Burgarella D., 2005, A&A, 435, 471
Inoue A. K., Iwata I., Deharveng J.-M., 2006, MNRAS, 371, L1
Inoue A. K. et al., 2011, MNRAS, 411, 2336
Inoue A. K., Shimizu I., Iwata I., Tanaka M., 2014, MNRAS, 442, 1805
Iwata I. et al., 2009, ApJ, 692, 1287
Izotov Y. I., Schaerer D., Thuan T. X., Worseck G., Guseva N. G., Orlitová I., Verhamme A., 2016, MNRAS, 461, 3683
Izotov Y. I., Worseck G., Schaerer D., Guseva N. G., Thuan T. X., Fricke K. J., Verhamme A., Orlitová I., 2018, MNRAS, 478, 4851
Janknecht E., Reimers D., Lopez S., Tytler D., 2006, A&A, 458, 427
Japelj J. et al., 2017, MNRAS, 468, 389
Kakiichi K., Dijkstra M., 2018, MNRAS, 480, 5140
Kakiichi K. et al., 2018, MNRAS, 479, 43
Kimm T., Cen R., 2014, ApJ, 788, 121
Ma X., Quataert E., Wetzel A., Hopkins P. F., Faucher-Giguère C.-A., Kereš D., 2020, MNRAS, 498, 2001
Mason C. A., Treu T., Dijkstra M., Mesinger A., Trenti M., Pentericci L., de Barros S., Vanzella E., 2018, ApJ, 856, 2
Meiksin A., 2006, MNRAS, 365, 807
Meštrić U. et al., 2020, MNRAS, 494, 4986 (M20)
Meurer G. R., Heckman T. M., Calzetti D., 1999, ApJ, 521, 64
Micheva G., Iwata I., Inoue A. K., Matsuda Y., Yamada T., Hayashino T., 2017, MNRAS, 465, 316
Momcheva I. G. et al., 2016, ApJS, 225, 27
Moutard T., Sawicki M., Arnouts S., Golob A., Coupon J., Ilbert O., Yang X., Gwyn S., 2020, MNRAS, 494, 1894
Møller P., Jakobsen P., 1990, A&A, 228, 299
Naidu R. P., Tacchella S., Mason C. A., Bose S., Oesch P. A., Conroy C., 2020, ApJ, 892, 109
Nakajima K., Ellis R. S., Robertson B. E., Tang M., Stark D. P., 2020, ApJ, 889, 161
Nestor D. B., Shapley A. E., Steidel C. C., Siana B., 2011, ApJ, 736, 18
Osterbrock D. E., 1989, Astrophysics of Gaseous Nebulae and Active Galactic Nuclei, University Science Books, Mill Valley, California
Ouchi M. et al., 2009, ApJ, 706, 1136
Paardekooper J.-P., Khochfar S., Dalla Vecchia C., 2015, MNRAS, 451, 2544
Parsa S., Dunlop J. S., McLure R. J., 2018, MNRAS, 474, 2904
Pentericci L. et al., 2018, A&A, 616, A174
Planck Collaboration XLVI, 2016, A&A, 596, A107
Reddy N. A., Pettini M., Steidel C. C., Shapley A. E., Erb D. K., Law D. R., 2012, ApJ, 754, 25
Reddy N. A., Steidel C. C., Pettini M., Bogosavljević M., Shapley A. E., 2016, ApJ, 828, 108
Rivera-Thorsen T. E. et al., 2019, Science, 366, 738
Robertson B. E., Ellis R. S., Furlanetto S. R., Dunlop J. S., 2015, ApJ, 802, L19
Rosdahl J. et al., 2018, MNRAS, 479, 994
Rudie G. C., Steidel C. C., Shapley A. E., Pettini M., 2013, ApJ, 769, 146
Saha K. et al., 2020, Nat. Astron., 4, 1185
Sawicki M. et al., 2019, MNRAS, 489, 5202
Seiler J., Hutter A., Sinha M., Croton D., 2018, MNRAS, 480, L33
Shapley A. E., Steidel C. C., Pettini M., Adelberger K. L., 2003, ApJ, 588, 65
Shapley A. E., Steidel C. C., Pettini M., Adelberger K. L., Erb D. K., 2006, ApJ, 651, 688
Shapley A. E., Steidel C. C., Strom A. L., Bogosavljević M., Reddy N. A., Siana B., Mostardi R. E., Rudie G. C., 2016, ApJ, 826, L24
Siana B. et al., 2007, ApJ, 668, 62
Siana B. et al., 2015, ApJ, 804, 17
Smith B. M. et al., 2018, ApJ, 853, 191
Steidel C. C., Pettini M., Adelberger K. L., 2001, ApJ, 546, 665
Steidel C. C., Bogosavlevic M., Shapley A. E., Reddy N. A., Rudie G. C., Pettini M., Trainor R. F., Strom A. L., 2018, ApJ, 869, 123
Straatman C. M. S. et al., 2016, ApJ, 830, 51
Tepper-García T., 2006, MNRAS, 369, 2025
Trebitsch M., Blaizot J., Rosdahl J., Devriendt J., Slyz A., 2017, MNRAS, 470, 224
Urrutia T. et al., 2019, A&A, 624, A141
Vanzella E., Siana B., Cristiani S., Nonino M., 2010, MNRAS, 404, 1672
Vanzella E. et al., 2012, ApJ, 751, 70
Vanzella E. et al., 2016, ApJ, 825, 41
Vanzella E. et al., 2018, MNRAS, 476, L15
Van Rossum G., Drake F. L., 2009, Python 3 Reference Manual. CreateSpace, Scotts Valley, CA
Virtanen P. et al., 2020, Nat. Methods, 17, 261
Weingartner J. C., Draine B. T., 2001, ApJ, 548, 296
Wise J. H., Cen R., 2009, ApJ, 693, 984
Yajima H., Choi J.-H., Nagamine K., 2011, MNRAS, 412, 411
Yamanaka S. et al., 2020, MNRAS, 498, 3095
Zackrisson E., Inoue A. K., Jensen H., 2013, ApJ, 777, 39

This paper has been typeset from a TEX/LATEX file prepared by the author.